Search for three-nucleon force effects in proton-deuteron elastic scattering

Ermisch, Karsten

Chapter 4

Data Analysis

In this chapter, the analysis of the data will be described. Since for the measurement of spin-observables, the determination of the polarisation degree of the beam is an essential component, first the analysis of the data taken with the KVI In-Beam-Polarimeter (IBP) will be discussed in detail in section 4.1.

For the measurement of the analysing powers and the cross sections of the process $^2\mathrm{H}(\vec{p}, dp)$, the BBS/ESN detection system has been used. The measurement of these observables was done during several experiments in the course of three years. The analysing powers at 135 and 150 MeV were measured in December 1999. The analysing powers at 120 MeV in March and at 170 MeV in April 2000. Then, the differential cross sections at 135, 170 and 190 MeV and the analysing power at 190 MeV were measured in June 2001. The differential cross sections and analysing powers at 108, 120 and 150 MeV were measured in December 2001. The measurement of a few data points at 190 MeV was repeated in April 2002 due to some problems during the first measurement. The analysis of all these data will be described in section 4.2.

The commissioning experiment of the reaction $\mathrm{H}(\vec{d}, dp)$ to determine the vector and tensor analysing powers and the differential cross section took place in February 2000. The analysis of these data will be outlined in section 4.3.

4.1 Analysis of the IBP Data

During most of the measurements of the vector analysing power with the BBS/ESN detection system, measurements of the degree of polarisation of the incoming proton beam were made in parallel using the IBP (see section 3.3). Therefore, the polarisation of the protons is known, in principle, for each data point of the analysing power A_y of the $^2\mathrm{H}(\vec{p}, dp)$ reaction, measured with the BBS/ESN detection system. In this section, the analysis of the IBP measurements will be described. Part of this is mentioned in reference [Bie01] and will be described here only briefly.

The polarisation degree p^i of the protons obtained from measurements in a plane with azimuthal angle ϕ^i was determined from the measurements of the IBP using

$$p^i = \frac{1}{A_y^p \cos\phi^i} \frac{L^i - R^i}{L^i + R^i}, \tag{4.1}$$

Table 4.1: *Final values of the polarisation for all six incident-beam energies for the reaction* $^2\mathrm{H}(\vec{p}, dp)$. *The values for these polarisations have been obtained according to equation* (4.6) *for those periods in which the polarisation was observed to be constant. The values given in this table can therefore deviate slightly from the polarisations given in the corresponding figures, where each data point is normalised individually to the hexapole-off measurement. The* χ^2 *given is the* χ^2 *of the fitted polarisation according to formula* (4.3). *Where numbers are given in brackets, the* χ^2 *of this fit deviates from* 1. *In the brackets, the values, obtained when forcing* $\chi^2 = 1$ *by increasing the uncertainties, are given.*

Beam Energy	Spin	p [%]	Δp [%]	χ^2
108 MeV, dσ, A_y				
	up1	56.2	1.6	0.5
	down1	–66.3	1.7	0.1
	up2	61.2	1.3 (2.0)	2.3 (1)
	down2	–58.5	1.3 (1.8)	1.8 (1)
	up3	48.8	1.4 (1.8)	1.7 (1)
	down3	–54.7	1.4 (2.1)	2.4 (1)
	down4	–61.0	1.4	1.3
120 MeV, A_y				
	off1	8.0	2.1	1
	down1	–58.0	2.2	1
	off2	6.6	1.6	0.3
	down2	-58.9	1.6	2.0
120 MeV, dσ, A_y				
	up1	55.1	3.3 (5.7)	3.1 (1)
	down1	–57.8	3.5 (5.5)	2.5 (1)
	up2	63.2	2.9 (5.3)	3.3 (1)
	down2	–64.6	2.9 (5.3)	3.3 (1)
	up3	54.9	2.0 (3.3)	2.6 (1)
	down3	–58.1	2.1 (3.4)	2.7 (1)
135 MeV, A_y				
	up1	59.6	1.2	0.9
	down1	–66.8	1.2	0.7
	up2	61.3	1.2	0.9
	down2	–64.0	1.2	0.9

continued on next page

continued from previous page

Beam Energy	Spin	p [%]	Δp [%]	χ^2
150 MeV, A_y				
	up	59.9	1.4	1.2
	down	–60.8	1.3	1.5
150 MeV, dσ, A_y				
	up	63.5	1.0	0.8
	down	–58.1	1.0	1.44
170 MeV, A_y				
	up1	59.7	0.9	0.6
	down1	–60.3	0.9	0.7
	up2	57.5	0.9 (1.3)	2.3 (1.0)
	down2	–54.7	0.9	0.5
	up3	59.3	2.2	1
	up4	50.6	0.9	0.6
	up5	59.9	1.6	1
	up6	57.1	1.8	0.77
	up7	56.9	1.9	0.61
	down3	–59.9	1.9	1
	down4	–48.9	0.8	0.6
	down5	–57.5	1.1	1
190 MeV, dσ, A_y				
	up1	49.2	1.7	0.13
	down1	–41.5	1.7	0.29
	up2	49.9	1.6	0.60
	down2	–43.4	1.6 (2.1)	1.72 (1.00)
	up3	49.8	1.6	0.29
	down3	–40.1	1.6 (2.0)	1.45 (1.00)
	up4	47.4	1.7	0.61
	down4	–45.3	1.6	0.46
190 MeV, dσ, A_y				
	up	68.0	0.5	0.12
	down	–67.3	0.5	0.1

where L^i and R^i symbolically represent the number of events counted on opposite sides of the beam axis in the plane with the azimuthal angle ϕ^i. Equation (4.1) corresponds to equation (3.3) in section 3.3. For the $0°$-plane, L corresponds to $\phi = 0°$ and R to $\phi = 180°$, as can be seen in figure 3.6 on page 36. For vector-polarised ions, only the instrumental asymmetry can be measured in the plane with $\phi^i = 90°$ and $\cos\phi^i$ should be omitted from equation (4.1) or any of the following equations. The analysing power A_y^p of the elastic proton-proton scattering reaction can be obtained with high precision from the existing fits to the world data such as that from the *Nijmegen* data base [nno]. The uncertainty on the prediction of the value of the analysing power from the Nijmegen potentials that was used in the analysis is $< 2\%$ [Tim02].

When determining the polarisation, the instrumental asymmetry of the IBP has to be taken into account. This is done by measuring the count rates L_0^i and R_0^i of each plane i with an unpolarised beam. The unpolarised beam is obtained by turning the hexapole magnetic field and the transition units of POLIS off (see section 3.1). The number of events measured with a polarised proton beam were then normalised to these *hexapole-off* runs, and the polarisation degree of the protons was calculated for each plane from [Sal73]

$$\begin{aligned} p^i &= \frac{1}{A_y^p \cos\phi^i} \frac{Y_L^i - Y_R^i}{Y_L^i + Y_R^i} \\ \text{with} \quad Y_L^i &= \frac{L^i}{L_0^i} \;\text{ and }\; Y_R^i = \frac{R^i}{R_0^i}. \end{aligned} \tag{4.2}$$

To obtain the polarisation degree of the protons from the results of the four planes of the IBP, a function

$$P(\phi) = A\cos(\phi + \alpha) \tag{4.3}$$

with the free parameters A and α was fitted to the polarisations obtained from the four planes. From this function, a normal and a sideways component of the polarisation was calculated,

$$\begin{aligned} P_n &= A\cos\alpha \\ P_s &= A\sin\alpha \end{aligned} \tag{4.4}$$

Ideally, the polarisation vector of the incoming protons should be normal to the horizontal plane and, therefore, $\alpha = 0$. During the experiments, the sideways component turned out to be $P_s < 1\%$ and could thus be neglected. In figures 4.1 to 4.6, the normal components of the up and down polarisations, corresponding to the strong and weak magnetic fields of POLIS, are plotted as a function of time for each energy. Each data point generally corresponds to a measurement of the proton-deuteron analysing power at a certain scattering angle. For some data points, several measurements of the polarisation were made. The uncertainties shown in these pictures contain only the statistical uncertainties which are due to the quantities L and R. The horizontal lines show the weighted averages of the polarisations for each energy over the whole time, as in figure 4.4, or over a time window, e.g. in figures 4.2, 4.3 and 4.5. The reason for making time windows at some energies will be given below with further details on the measurements at each beam energy.

To obtain an estimate for the stability of the beam polarisation, the individual polarisation measurements were averaged. When calculating the weighted average of the data points shown in figures 4.1 - 4.6, as

$$P_n(\text{Energy}) = \frac{1}{\sum_k^N \left(\frac{1}{\Delta p_n^k}\right)^2} \sum_k^N \frac{P_n^k}{(\Delta p_n^k)^2}$$
$$\chi^2 = \frac{1}{N-1} \sum_k^N \left(\frac{P_n - P_n^k}{\Delta p_n^k}\right)^2 \tag{4.5}$$

where P_n^k corresponds to the individual measurements, the statistical error that is due to the hexapole-off run should not be propagated in the individual uncertainties Δp_n^k. Otherwise, the uncertainty of the hexapole-off measurement would contribute to every data point and to the χ^2 as often as there are data points, leading to a wrong mean and a too small χ^2. The statistical errors due to L_0 and R_0 have therefore not been propagated in the calculations of the data points shown in figures 4.2 to 4.6, even though the polarisation values were calculated according to equation (4.2). The results of the weighted averages and the corresponding χ^2, obtained according to formula (4.5), are also shown in these figures.

If the polarisation turned out to be constant within the statistical fluctuations for one energy over a certain time window, with $\chi^2 \approx 1$, as is the case in figures 4.1 to 4.6, the polarisation could have been determined during this time with higher accuracy. In such a case, all the counts for L and R for each plane can be added and the polarisation degree for the different magnetic fields can be determined with a higher accuracy from these sums. These sums have to be normalised to the hexapole-off runs. In this way, also the statistical uncertainties due to L_0 and R_0 can be taken into account in the correct way. The polarisation degrees of the protons were then determined by calculating

$$P_i = \frac{1}{A_y^p \cos\phi^i} \frac{\sum_j L_j^i/L_0^i - \sum_j R_j^i/R_0^i}{\sum_j L_j^i/L_0^i + \sum_j R_j^i/R_0^i} \tag{4.6}$$

where i indexes the planes at $0°$, $45°$, $90°$ and $135°$ and $\sum_j$ is the sum over all counted events. Again, the normal and sideways components of the polarisations were obtained from a fit of the P_i, as has been described before. The final values for the polarisations that were used to calculate the analysing powers of the reaction $^2\text{H}(\vec{p}, dp)$ are given in table 4.1. The details relevant for a specific beam energy are given below.

As can be seen in table 4.1, the uncertainty in the polarisations is in general $< 3\%$. To account for possible systematic uncertainties, it was set to $\Delta p/p = 3\%$. This 3% systematic uncertainty also includes the uncertainty of $< 2\%$ in the prediciton from the Nijmegen potential. Exceptions are at the second measurement of 120 MeV beam energy and at part of the measurements at 190 MeV, where the relative uncertainty in the polarisations is larger than the value given above. However, as will be shown later, the good agreement of the results of the analysing power from different measurements shows, that the uncertainty in the polarisation is probably smaller than the estimation made here. Further details about the propagation of the uncertainty in the polarisation into the measured observables will be given in section 4.2.

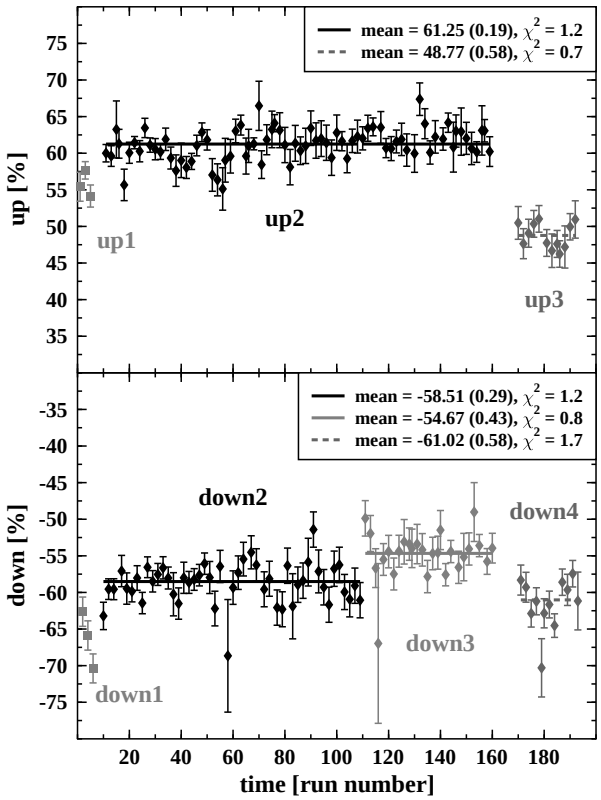

Figure 4.1: Shown is the beam polarisation as a function of time at 108 MeV bombarding energy. The time is given in run numbers. The figure covers a time span of about 24 hours of measurement. Each polarisation value was obtained according to equations (4.2) *and* (4.4)*. The solid and dashed lines show the weighted average of these polarisations. The results and the* χ^2 *obtained are given in the plot. In these averages, the statistical error due to the hexapole-off runs has not been propagated. To accentuate different running periods different shadings have been used.*

Analysis at 108 MeV The values for the polarisation obtained from the IBP measurements at 108 MeV beam energy are shown in figure 4.1. As can be seen in this figure, the polarisation degree of the weak field changed during the middle of the run. Both weak and strong fields changed in the beginning and before the last part of the measurement. Therefore, three different polarisation values were obtained for up polarisation, and four for down polarisation.

Analysis at 120 MeV The results for the polarisation obtained from the IBP measurements at a beam energy of 120 MeV for both measurements are shown in figure 4.2. When the measurement of the vector analysing power at this energy was performed, the strong magnetic field of the polarised ion source, which delivers protons with up polarisation, failed. According to equation 4.15, the vector analysing power can also be determined from measurements with down and off

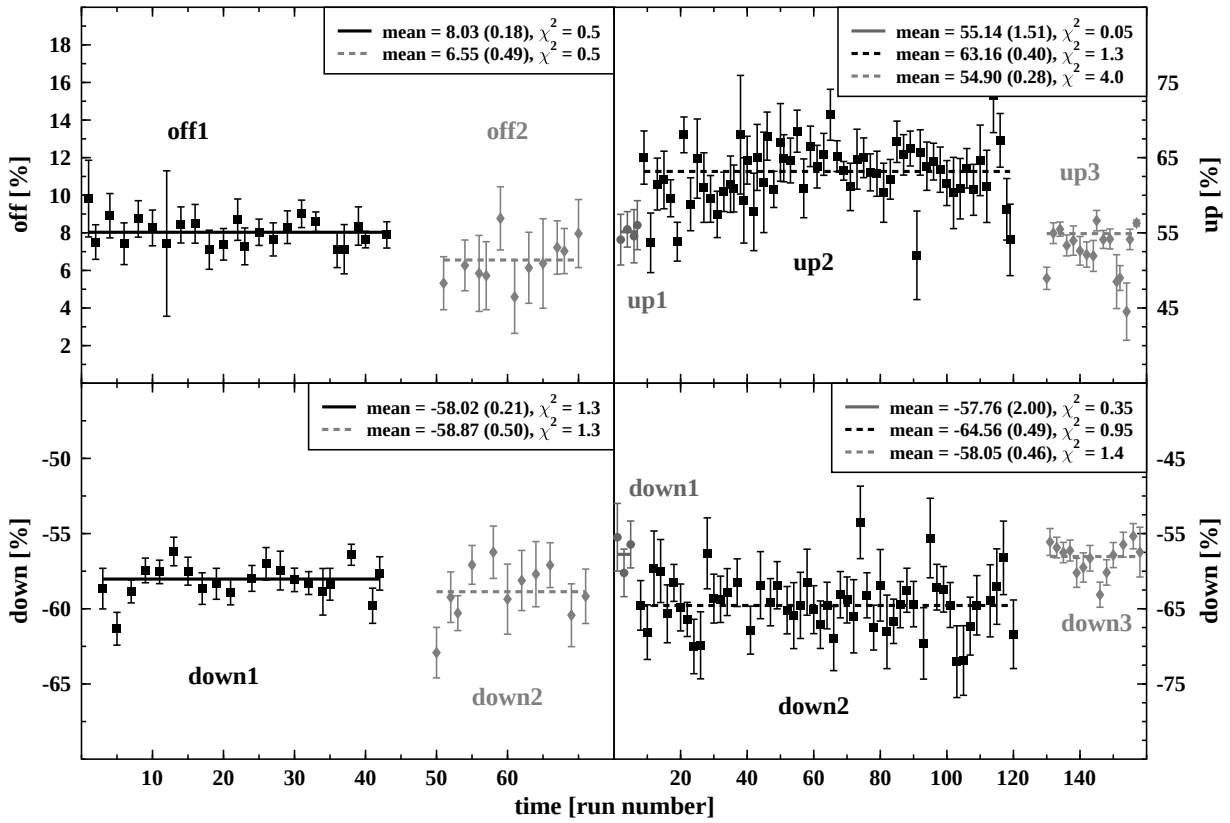

Figure 4.2: Shown are the beam polarisations as a function of time for 120 MeV bombarding energy. The left picture shows the polarisation during the measurement of the analysing power. A break was made during the experiment, after which the behaviour of the polarised ion source changed. On the right, the polarisation during the measurement of the differential cross section for this beam energy is shown. The last part of this measurement was done one day later than the first part. In both pictures, the time span shown corresponds to about 24 hours of measurement. Further details can be found in the caption of figure 4.1.

polarisation, although the accuracy will decrease. Therefore, the analysing power at 120 MeV was determined using the polarisation values for these spin states. As already remarked earlier, the polarisation value for spin off has an offset and is therefore different from zero. As can be seen in figure 4.2, the polarisations for both, spin down and spin off were stable during two time windows. Therefore, for the determination of the analysing power, the mean values of the polarisation degrees during the corresponding time windows were used.

Also shown in figure 4.2 are the polarisation values determined during the measurement of the differential cross section. During this experiment, also the analysing power was measured a second time. After the first measurements, the polarisation changed for both fields. The same happened during the last part, which was measured about a day later than the rest.

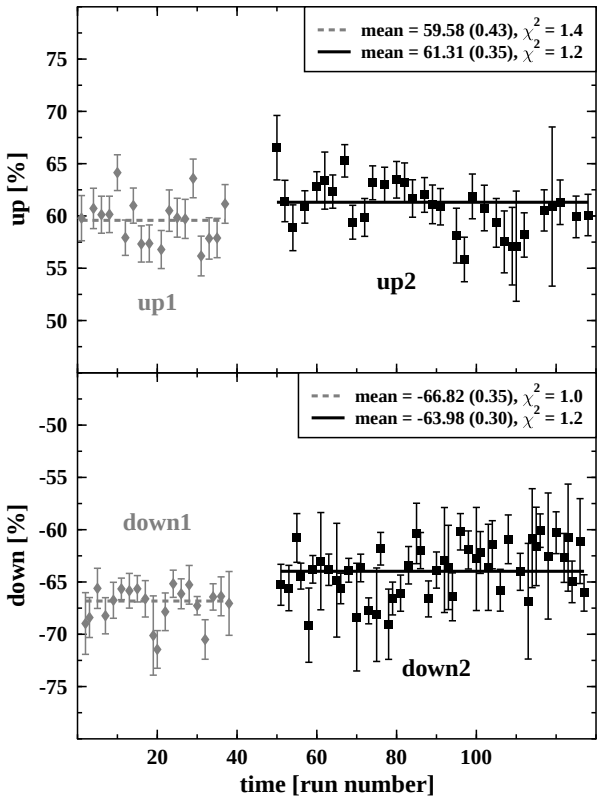

Figure 4.3: Beam polarisation at a bombarding energy of 135 MeV as a function of time. The measurements of the points denoted by diamonds were made on a different day than the other measurements, and therefore treated separately when calculating the average. The first part corresponds to a time span of six hours, the second part to a time span of 14 hours of measurement. Further explanations can be found in the caption of figure 4.1.

Analysis at 135 MeV In figure 4.3, the polarisation during the measurement at a bombarding energy of 135 MeV is shown. The different time windows shown correspond to measurements made on two different days. The polarisations for these two days were therefore determined independently.

Analysis at 150 MeV The results of the analysis of the polarisation for measurements at 150 MeV are shown in figure 4.4. As can be seen, during both measurements of the vector analysing power and the differential cross section, the polarisations for spins up and down were stable during the whole experiment within the statistical uncertainties.

Analysis at 170 MeV In figure 4.5, the polarisations measured during the 170 MeV run are displayed. As can be seen, the time span can be divided into three parts. During the first phase, the polarisations of both spin up and spin down were stable. At the end of this phase, the POLIS

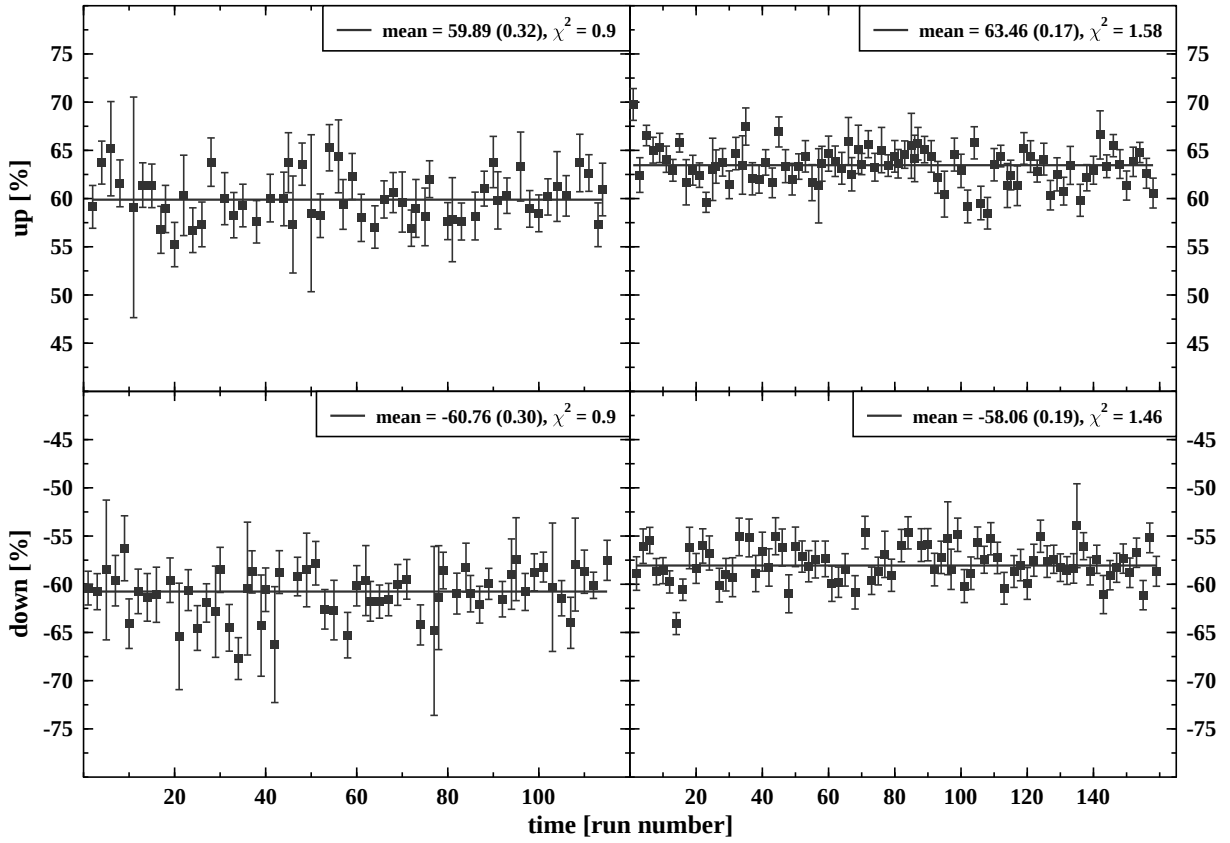

Figure 4.4: Beam polarisation at a bombarding energy of 150 MeV as a function of time. On the left side, the polarisation during the measurement of the vector analysing power is shown. On the right side, the polarisation values are shown that were obtained during the measurement of the differential cross section, during which the analysing power was measured a second time. Both pictures cover a time span of about 16 hours. Further explanations can be found in the caption of figure 4.1.

failed and measures had to be taken by the cyclotron operator. After the POLIS started working again, the degree of polarisation of spin down had changed, but was again stable (second phase). Also, the polarisation of spin up was constant. Therefore, the mean polarisation was established for both periods of time separately. At the end of the second phase, the POLIS failed again. During the whole third phase that followed, the polarisation of neither spin up nor spin down was stable anymore, as can be seen in figure 4.5. However, the polarisation was stable for a few measurements made directly after each other. For these measurements, the average value of the polarisation was used for determining the analysing power of the points measured at that particular time.

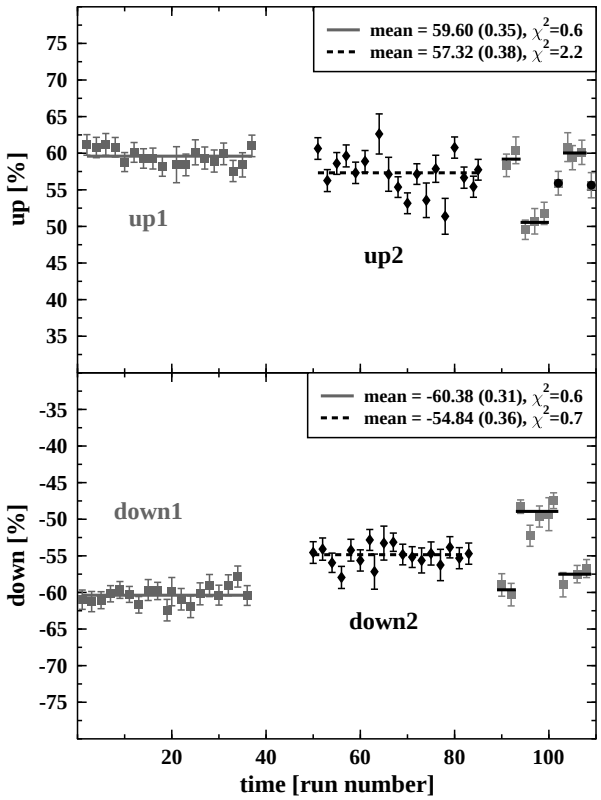

Figure 4.5: Beam polarisation at a bombarding energy of 170 MeV as a function of time. The complete picture covers about 24 hours of measurement time. The time is divided into three phases, according to different conditions of the POLIS. In the last phase, weighted averages of the polarisation were taken, where possible, denoted by lines. The two measurements of the up polarisation, denoted by black dots, in the last phase, were not used in determining the averages and were taken as individual measurements of polarisation. The corresponding measurements of the analysing power of the $^2\mathrm{H}(\vec{p}, dp)$ *reaction were analysed using these measured polarisation values.*

Analysis at 190 MeV In figure 4.6, the polarisation measured at 190 MeV is shown as a function of time. On the left hand side, the polarisations during the first measurement are shown. The whole time is divided into four phases, according to several measurements done with the hexapoles turned off. As can be seen in figure 4.6, the down polarisation differs for each separate normalisation measurement and four different values for the down polarisation were obtained. For the up polarisation, the first three phases have the same value, and the polarisation degree measured during the fourth phase was used separately. Also shown in figure 4.6 are the results for the polarisation degree during the second measurement of a few points for the differential cross section and the analysing power of the reaction $^2\mathrm{H}(\vec{p}, dp)$. As can be seen in figure 4.6, the polarisation remained constant during this experiment.

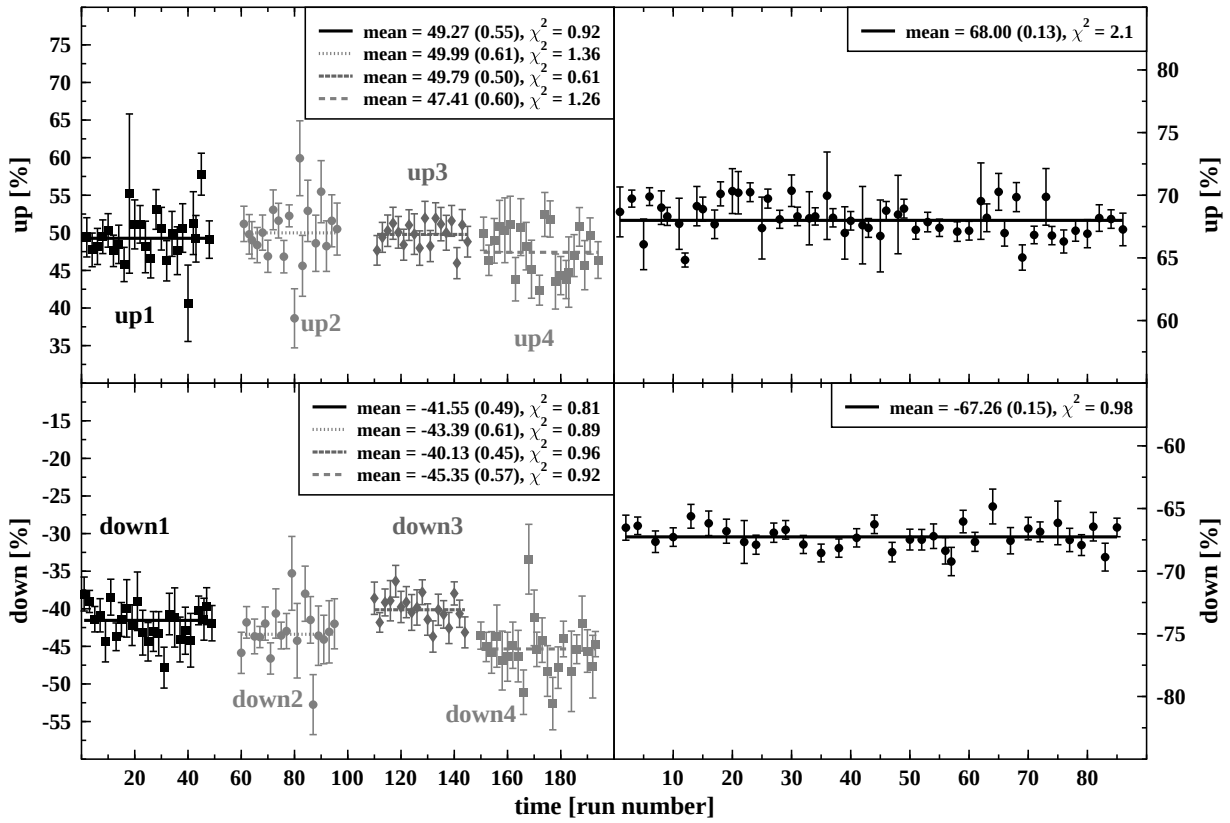

Figure 4.6: Beam polarisation at a bombarding energy of 190 MeV as a function of time. On the left hand side, the polarisation during a first measurement at this beam energy is shown. The time is divided into four phases, according to four different normalisation measurements with the hexapoles turned off. The complete time span covers about 24 hours of measurement. For the up polarisation, a weighted average of the first three phases was used. For the down polarisation, four different polarisation values, according to the four different normalisation measurements, were obtained. On the right side, the polarisation during a second measurement at 190 MeV beam energy is shown. The whole time covered here corresponds to about 11 hours.

4.2 Analysis of the BBS/ESN Data

In the following subsections, the analysis of the data obtained with the BBS/ESN detection system for the reaction $^2\mathrm{H}(\vec{p}, dp)$ will be described. The determination of the differential cross section and the analysing power from this analysis will be described in subsection 4.2.5.

As explained in section 3.4, measurements with the BBS/ESN detection system were made at several laboratory scattering angles between $14°$ and $53°$, measuring alternately the protons and the deuterons with the spectrometer. The measurements were performed in steps of $3°$. Measurements for the deuteron were also made at scattering angles down to $5°$, also in steps

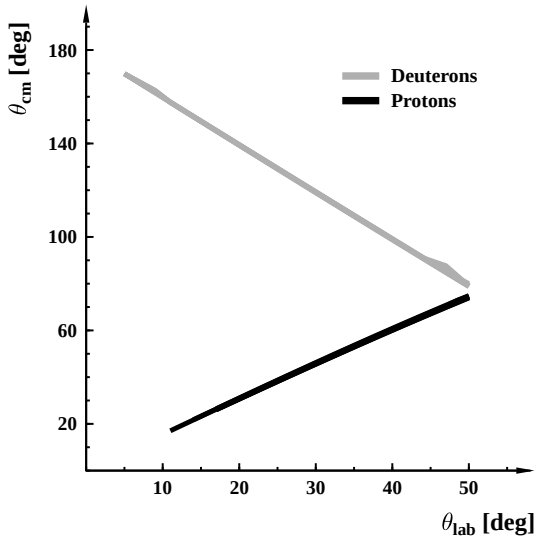

Figure 4.7: θ_{lab} of the BBS/ESN detection system versus θ_{cm}. The bands shown are due to the different kinematics for different incident-beam energies.

of 3°. In this way, a centre-of-mass scattering angular range between 30° and 170° could be covered. The angular coverage for all beam energies is shown in figure 4.7. There, the centre-of-mass angular range is plotted versus the laboratory scattering angle of protons and deuterons.

At each kinetic energy except for 120 MeV, the analysing power was determined at each scattering angle from measurements using the up and down polarisations. For comparison, also measurements using the off polarisation were done for each scattering angle at each energy, expect at 190 MeV. At 120 MeV bombarding energy, the strong-field transition unit of POLIS, providing protons with spin up, failed. Instead, off and down polarisations were used for the determination of the analysing power. At this beam energy, the measurement of the analysing power was repeated using the spin states up and down. The results of both measurements agree very well.

At 108, 120, 150 and 190 MeV, the differential cross section was measured with polarised beams from POLIS and was deduced from measurements with up and down polarisation. For the measurement of the differential cross section at 135 and 170 MeV incident-beam energy, the unpolarised ion source was used.

The analysis of the data obtained with the BBS/ESN detector was split into two parts. First, the raw data was analysed and certain variables, which will be explained in more detail, were calculated. These variables were then stored in ntuples for further and more convenient data analysis, using the software packages *HBOOK* and *PAW* developed at CERN [HBO95, PAW95]. In the following subsection, the first part of the data analysis will be described briefly. It follows mainly the analysis used by the EuroSuperNova collaboration. More details about the analysis can, therefore, be found in [Han01, Wör01].

4.2.1 Pre-analysis of the Raw Data

In the analysis of the raw data, the trajectories of the particles at the focal plane were constructed from the TDC signals of the VDCs. These were the cartesian coordinates X_d and Y_d and the relative scattering angles θ_d and ϕ_d with respect to the central ray at the focal plane. Further, the x position corrected for kinematical broadening at the focal plane, X_f, was calculated [Han01]. From the TDC-signals of the two scintillator planes *S1* and *S2*, the time-of-flight (ToF) between the two planes and time-over-threshold (ToT) signal for each scintillator paddle could be calculated.

Knowing the crossing point of the particle in the focal plane, it is possible to ray-trace the particle back through the spectrometer and calculate its crossing point at the entrance of the BBS. This crossing point is given in horizontal (Θ) and vertical (Φ) angles. The names of the vertical and horizontal angles are used according to the standard notation for spectrometers. However, one should take into account that these cartesian angles do not correspond to real spherical angles. The azimuthal and polar scattering angles φ and ϑ of the particles can be obtained from these quantities with

$$\begin{aligned} \vartheta &= \arccos(\cos(\Theta_{\mathrm{BBS}} + \Theta) \cdot \cos\Phi) \\ \varphi &= \arctan\left(\frac{\sin(\Theta_{\mathrm{BBS}} + \Theta)}{\tan\Phi}\right) \end{aligned} \tag{4.7}$$

as explained in appendix B. To obtain the analysing power, the calculation of the solid angle was not necessary and the standard angles Θ and Φ were sufficient to make cuts on the opening angle of the BBS. For the analysis with respect to the differential cross section, the whole BBS opening was used. This will be explained in more detail in subsection 4.2.2.

The variables $X_d, Y_d, \theta_d, \phi_d, \Theta, \Phi$ and the time-of-flight were stored in the ntuple. In addition, part of the information stored in the scaler units, as described in section 3.4, was read out and written to the same ntuple. The scaler information stored in the ntuples consisted of the live-time of the data-acquisition, the collected charge and the polarisation bit.

4.2.2 Analysis of the Ntuples

At each bombarding energy, measurements were made at about 30 different settings, which correspond roughly to 15 measurements with the protons from the reaction $^2\mathrm{H}(\vec{p}, dp)$ entering the spectrometer, and about the same number of measurements for the deuterons from the same process. At six bombarding energies, this adds up to roughly 200 measurements. Since the vector analysing powers and the differential cross sections were measured separately for most energies (see section 3.4), the number of data points, each of which had to be analysed separately, doubles.

After a first raw analysis of the data, using the standard BBS/ESN methods as was described above, the pre-analysed data were stored in ntuples. For the purpose of analysing the data, a program was written to read in the ntuples of each data point measured, apply the necessary cuts to the data, and calculate the analysing power and the differential cross section. For each data point, an input file was provided with the specific information, like beam energy, scattering angle and the boundaries for cuts. Since these input files had to have an identical scheme, this

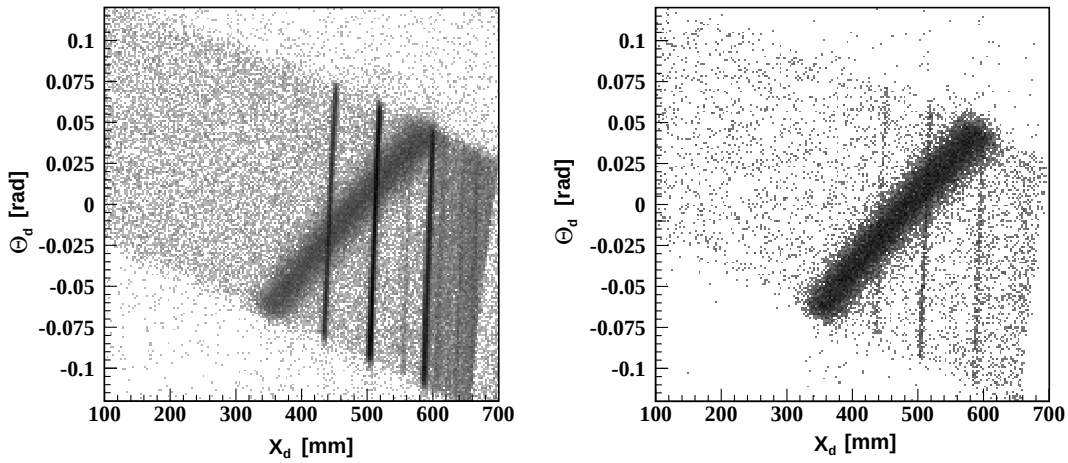

Figure 4.8: Two-dimensional spectra showing variables determined at the position of the focal plane. Shown is the relative angle θ_d with respect to the central trajectory versus the position of the particle in the x plane of the first VDC. Both spectra were taken for a setting at 150 MeV beam energy, where the deuteron emerging from the $^2\mathrm{H}(\vec{p}, dp)$ reaction is scattered to a laboratory angle of 41°. The left spectrum was recorded using a singles trigger, the right spectrum using a coincidence trigger. Further explanations are given in the text.

procedure ensured, that the same method of analysis was supplied to each data point. In the following subsections, the procedure employed to analyse the data using the ntuples will be laid out.

Event Selection in the Focal Plane

To select the events stemming from the reaction $^2\mathrm{H}(\vec{p}, dp)$, two-dimensional spectra of the focal plane coordinates X_d and θ_d were used. In figure 4.8, examples of these spectra are shown using the singles trigger, as described in section 3.4, and the coincidence trigger, for the same setting. The spectra in this figure show the scattering angle relative to the central trajectory θ_d at the focal plane versus the position of the particle in the x plane of the first VDC. In these spectra, deuterons emerging from the reaction $^2\mathrm{H}(\vec{p}, dp)$ were recorded in the BBS/ESN detection system at a laboratory scattering angle of 41° and a beam energy of 150 MeV. The broad dark band is the locus of the deuterons. The narrow dark bands, which can be seen in both spectra, are due to protons emerging from the reaction $^{12}\mathrm{C}(p, p')^{12}\mathrm{C}$. At some other scattering angles, background events stemming from the reaction $^{12}\mathrm{C}(p, d)^{11}\mathrm{C}$ were recorded. Since the mass ratio between deuterons and protons is rather small, as compared to the mass ratio between carbon and proton, particles emerging from the reaction $^2\mathrm{H}(\vec{p}, dp)$ will have a larger kinematical broadening in the focal plane, as can be seen in figure 4.8. To simplify the event selection in the focal plane, a virtual focal plane was used [Han01]. In this virtual focal plane, shown in figure 4.9 for the same setting as figure 4.8, the distribution of momenta of the outgoing particle is corrected for

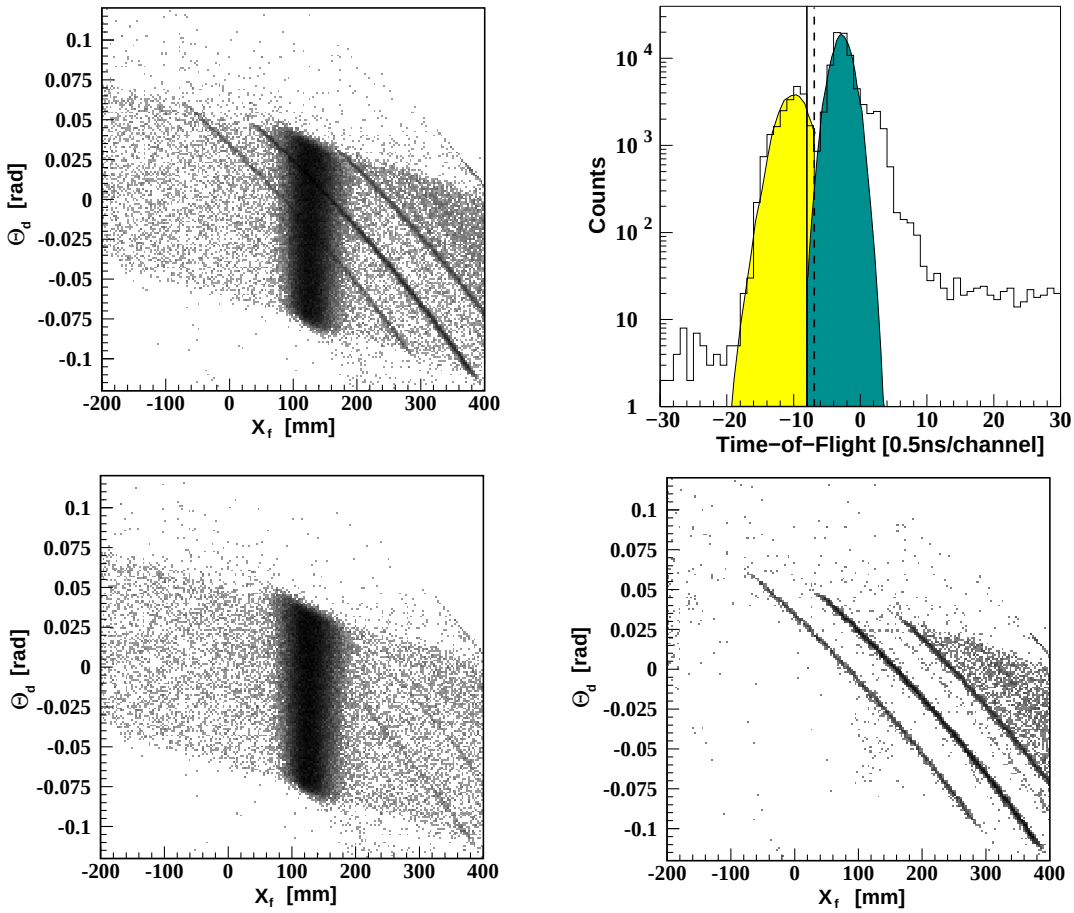

Figure 4.9: Shown are two-dimensional spectra at the virtual focal plane measured at 150 MeV beam energy for the same settings as in figure 4.8. In the upper-left figure, the virtual focal plane spectrum is shown with events from the reactions $^2\mathrm{H}(\vec{p},dp)$ *and* $^{12}\mathrm{C}(p,p')^{12}\mathrm{C}$*. In the upper-right figure, the ToF spectrum is shown with two peaks, a light-shaded one (left), corresponding to the ToF of protons emerging from the reaction* $^{12}\mathrm{C}(p,p')^{12}\mathrm{C}$ *and a dark-shaded peak (right), corresponding to deuterons emerging from the* $^2\mathrm{H}(\vec{p},dp)$ *reaction. In the lower-left figure, the spectrum of the virtual focal plane is shown, where the deuterons have been selected by making a cut on the dark-shaded peak. The actual cut was made between the solid line and the right edge of the histogram. The lower-right figure shows the spectrum with a selection on the protons emerging from the reaction* $^{12}\mathrm{C}(p,p')^{12}\mathrm{C}$*. Here, the actual cut was made between the dashed line and the left edge of the histogram.*

the kinematics of the reaction of interest, $^2\mathrm{H}(\vec{p},dp)$, and hence the events due to deuterons are assembled in one vertical band. The advantage in this case is that a one-dimensional cut can be applied to the position X_f in the virtual focal plane. Otherwise, one would have to set a two-dimensional cut in the real x position X_d, with a dependence on θ_d. To reduce the background

stemming from the reaction $^{12}\mathrm{C}(p,p')^{12}\mathrm{C}$, as is shown in figures 4.8 and 4.9, the ToF between the two scintillator planes *S1* and *S2* was used. Since deuterons and protons with the same momentum-to-charge ratio, and thus the same magnetic rigidity, have different velocities, the ToF between *S1* and *S2* differs and can be used to separate them. Furthermore, the ToF spectrum, where the two peaks corresponding to events from the reactions $^{2}\mathrm{H}(\vec{p},dp)$ and $^{12}\mathrm{C}(p,p')^{12}\mathrm{C}$ can be distinguished, is also shown in figure 4.9. Both peaks were fitted with a gaussian distribution, to help place the cuts properly. The actual cuts were made between one of the lines in the centre and the edge of the histogram in order not to cut away valid events of either reaction. The two two-dimensional spectra of the virtual focal plane obtained with these cuts in the ToF spectrum are shown at the bottom of figure 4.9.

Another source of background at a laboratory scattering angle around 50° was the reaction $^{2}\mathrm{H}(\vec{p},dp)$ itself. In this angular range, protons and deuterons from this reaction are scattered into the same angular range with a similar magnetic rigidity. Therefore, also with a coincidence setup, both particles will be detected simultaneously with the BBS/ESN. In figure 4.10, an example of a two-dimensional spectrum measured at the focal plane is shown where both the outgoing protons and deuterons of the reaction $^{2}\mathrm{H}(\vec{p},dp)$ are measured with the focal-plane detection system. Here, too, the selection using the ToF can be used to discriminate between protons and deuterons.

The method of setting cuts in the virtual focal plane to determine the total number of detected particles of interest was used in the analysis of the data published in reference [Erm01] of the analysing powers at the energies 120, 135, 150 and 170 MeV. The spectra corrected for kinematical broadening still display peaks with a gaussian distribution, as can be seen in figure 4.11. By setting cuts on the x position in the virtual focal plane, part of the good events are also cut away in the tails of the distribution. Since the analysing power is obtained from a difference between two cross sections, the events in the tails of the distribution hardly contribute. However, for the measurements of the differential cross section the method of analysing the data had to be improved. In a slightly modified version of the analysis software, a superposition of a gaussian curve and a polynomial background was fitted to the data in the virtual focal plane, as is shown in figure 4.11. The starting parameters of the fit were chosen such that a gaussian would be fitted to the peak corresponding to the events stemming from the $^{2}\mathrm{H}(\vec{p},dp)$ reaction and a polynomial to the background events. For the background, it was sufficient to use a polynomial of third order or less. The gaussian was then integrated over a large region to obtain the number of collected events. The fit had to be applied to each spin state separately. This method of event analysis was employed for all cross-section measurements and the measurements of the analysing power at 108 MeV and 190 MeV. A comparison between this method of analysis with the method using cuts in the focal plane showed, as expected, no difference in the results obtained for the analysing power.

The background in the focal plane was mainly due to the carbon contained in the polyethylene matrix of the target. At angles where bands from the reactions $\mathrm{H}(p,p)\mathrm{H}$ or the deuteron break-up were recorded, these were located at a different region of the focal plane. To check, whether the background due to carbon was subtracted sufficiently when using a polynomial fit, as described above, measurements were done using a pure carbon target. The spectra of X_f recorded during those measurements was fitted with a polynomial. The result of that fit was, after correcting

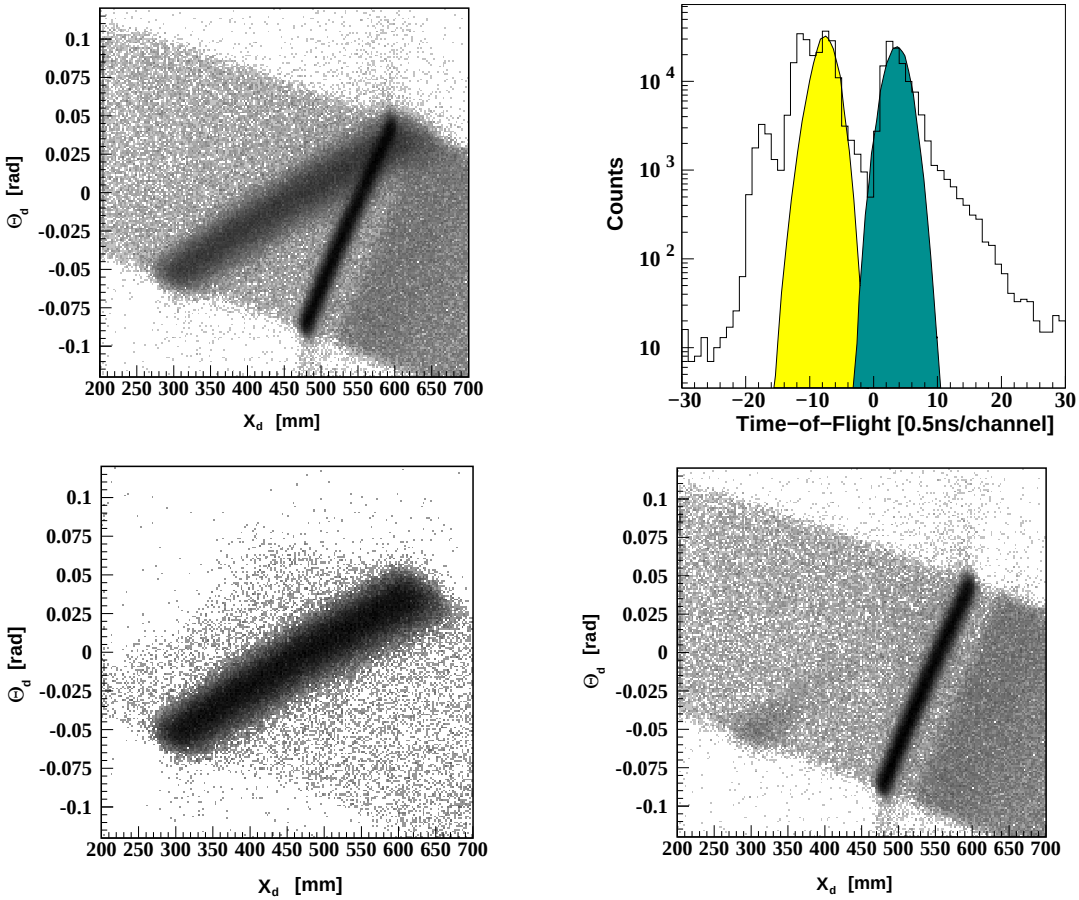

Figure 4.10: Shown are events at a bombarding energy of 150 MeV for a scattering angle of $50°$*. At this angular setting, protons and deuterons emerging from the* $^2\mathrm{H}(\vec{p}, dp)$ *reaction are both scattered to the same angle with a similar magnetic rigidity. Furthermore, background stemming from the* $^{12}\mathrm{C}(p, p')^{12}\mathrm{C}$ *reaction has been recorded. In the upper-left figure, the two-dimensional spectrum of the incidence angle versus position at the focal plane can be seen. The broad dark band represents the scattered deuterons, the narrow dark band shows the protons from the same reaction. In the upper-right figure, the ToF spectrum for this reaction is shown, with the left (light-shaded) peak corresponding to protons and the right (dark-shaded) peak corresponding to deuterons. In the lower-left figure, the deuteron band has been selected by a cut on ToF and in the lower-right figure the proton band.*

for the different luminosity, subtracted from the corresponding spectrum measured with a CD_2 target. An example is shown in figure 4.12. In the upper left panel, a one-dimensional histogram of the recoil-corrected focal-plane position is shown. This histogram was recorded for a setting at 170 MeV incident-beam energy with the deuteron emerging from the reaction $^2\mathrm{H}(\vec{p}, dp)$ entering the BBS at $38°$. In this histogram, the result of a fit using a sum of a gaussian and a polynomial, and the result for the polynomial part of the fit are shown. In the histogram shown in the lower-left

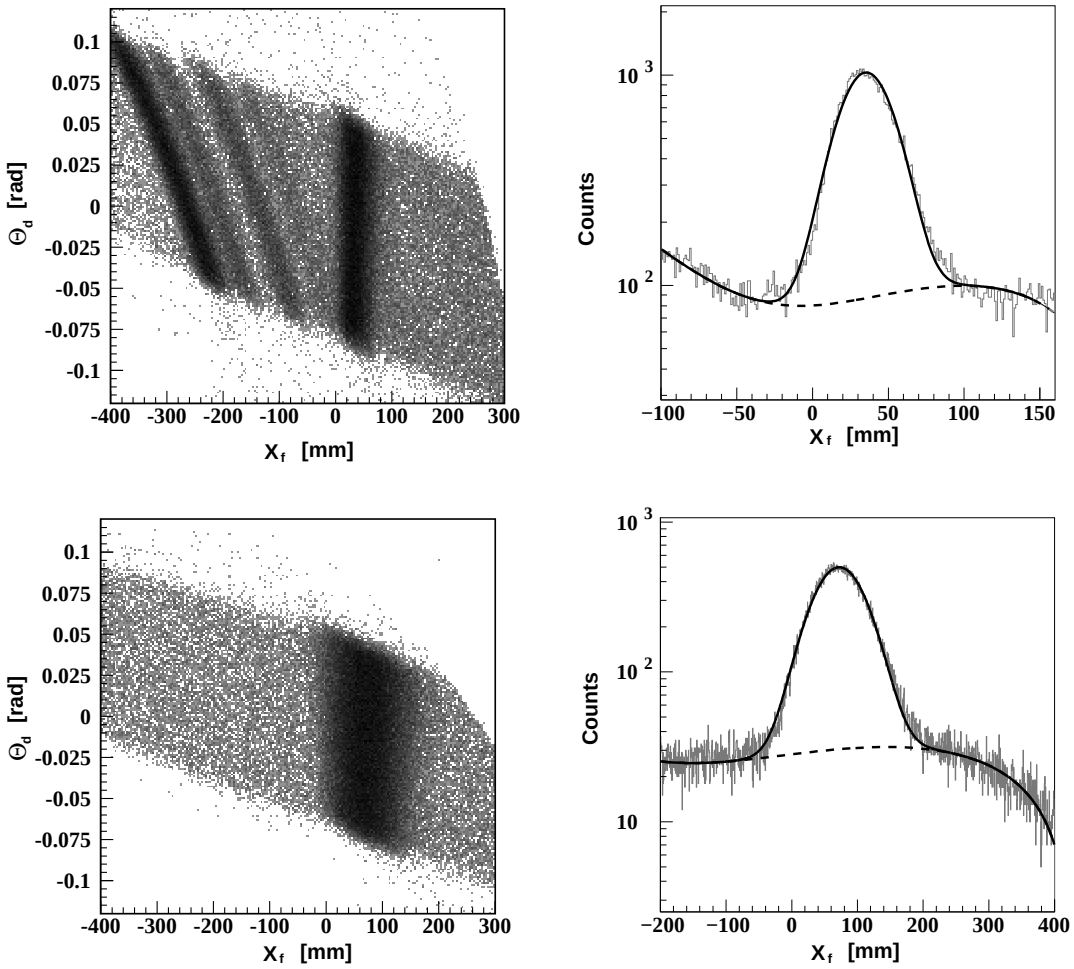

Figure 4.11: Examples of fits of the spectra in the virtual focal plane. The spectra in the upper part were recorded for a setting at 108 MeV beam energy with the deuteron emerging from the reaction $^2\mathrm{H}(\vec{p}, dp)$ *and entering the BBS at a laboratory scattering angle of* $26°$*. On the left side, the correlation between* θ_d *and* X_f *is shown. The skewed bands seen in this 2-dimensional plot stem from the reaction* $^{12}\mathrm{C}(p, d)^{11}\mathrm{C}$*. No cuts were made for the event selection. On the right side the projection onto* X_f *together with the results of the fit (dark line) are shown. The fitted function consists of the sum of a gaussian and a third-order polynomial. The dashed line shows the result of the polynomial fit to the background. In the lower part, the same spectra are shown for a setting where deuterons were measured at a scattering angle of* $41°$*. Here, a ToF cut was used to remove background stemming from the reaction* $^{12}\mathrm{C}(p, p')^{12}\mathrm{C}$*.*

panel of figure 4.12, the polynomial has been subtracted from the measured spectrum shown in the upper-left panel. In the upper-right figure, a histogram of a measurement for the same setting but using a carbon target is shown. This histogram was fitted with a third-order polynomial. In the lower-right panel, this polynomial was subtracted, after a proper normalisation, from the

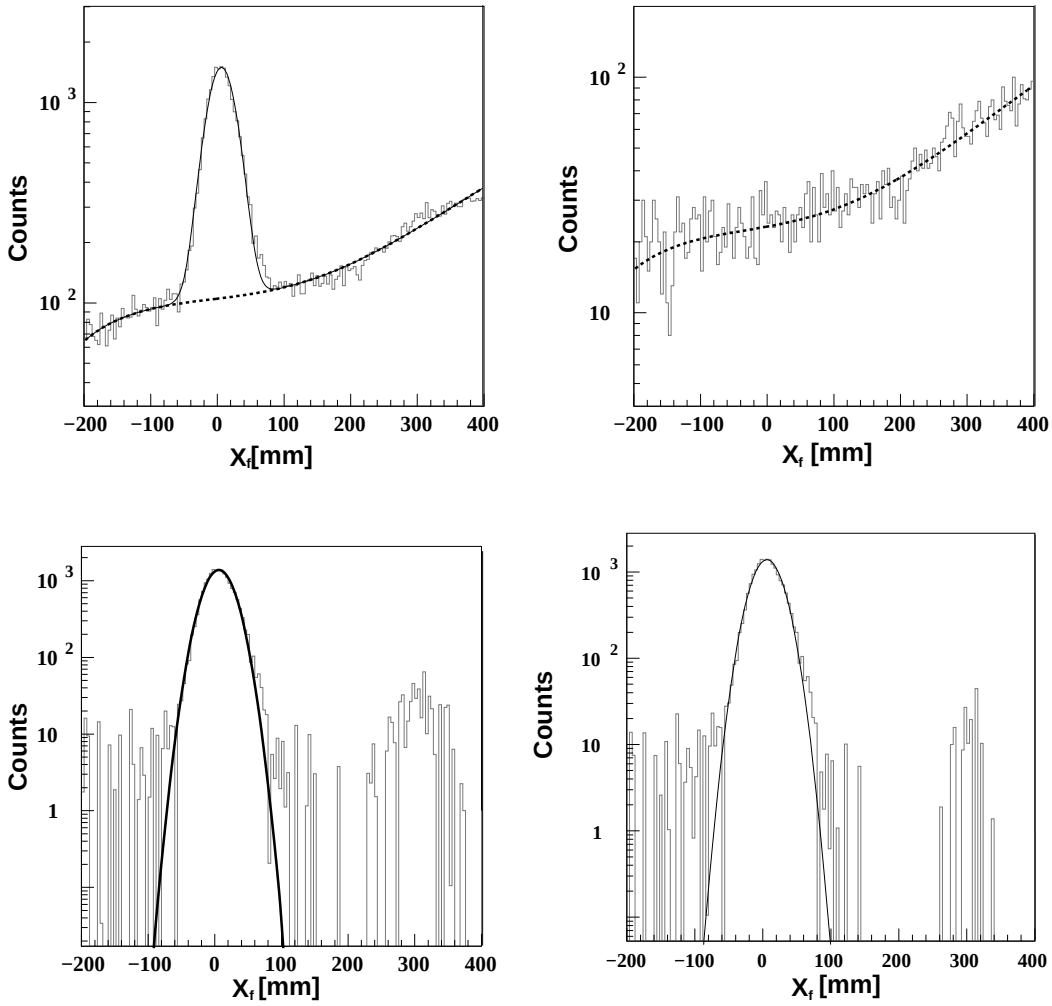

Figure 4.12: Background subtraction for spectra of the virtual focal plane. The spectra were recorded for a setting at 170 MeV incident-beam energy and a laboratory angle of 38°*. In the upper-left panel, a spectrum of the position* X_f *is shown with the deuteron entering the BBS. Also shown are the result of the gaussian+polynomial fit and the result of the polynomial fit on its own. In the lower-left panel, a histogram is shown where the polynomial fit has been subtracted from the spectrum shown in the upper-left panel. In the upper-right panel, a spectrum for the same settings as in the upper-left panel, but taken with a pure carbon target is shown together with a polynomial fit of the spectrum. In the lower-right panel, a histogram is shown where the polynomial fit of the spectrum taken with the carbon target has been subtracted from the histogram shown in the upper-left panel.*

histogram shown in the upper-left figure. The difference between the two histograms shown in the lower panels in figure 4.12 is negligible, showing that the method of fitting is indeed sufficient to subtract the carbon background.

Further Background Subtraction

As was mentioned before, the measurements of the analysing power at 120, 135, 150 and 170 MeV were analysed with the method of setting cuts in the virtual focal plane. For some of these measurements, background in the focal plane could not be distinguished from the good events using the ToF information. This is due to the fact that identical particles from different reactions enter the BBS with the same magnetic rigidity. To remove the background contribution, a region of the virtual plane has to be selected where the background is uniform and of the same height as in the 'good' region. Background, which could not be reduced with a ToF cut, was dominant at BBS angles around 20° with protons entering the BBS. At these angles, protons emerging from the reaction $^2\mathrm{H}(\vec{p}, dp)$ overlap with protons emerging from the reaction $^{12}\mathrm{C}(p, p')^{12}\mathrm{C}$ in the focal plane. As the BBS was moved to larger angles, protons due to scattering from deuterium moved to the low-momentum side of the focal plane faster than protons due to scattering from carbon. At laboratory angles around 40°, the protons emerging from the $^2\mathrm{H}(\vec{p}, dp)$ reaction overlapped with the continuum of the reaction $^{12}\mathrm{C}(p, p')^{12}\mathrm{C}$. As is shown in appendix C, for background which does not depend on the polarisation, the relative error made when calculating the analysing power corresponds to the relative amount of the background with respect to the number of real events. Therefore, if the background/signal ratio in the coordinate X_f was $< 1\%$, it was not corrected for. In this case, the error made in the analysing power was also $< 1\%$, which is in general far less than the statistical error. If the background was higher and could not be removed by cuts on the ToF, it was subtracted to determine the real number of events from the $^2\mathrm{H}(\vec{p}, dp)$ reaction. For the determination of the differential cross sections, the background was subtracted by fitting a gaussian to the good events, as it was described earlier.

Time Cuts

In some cases, especially during the measurements at beam energies of 135 MeV and 170 MeV, POLIS and the RF of AGOR fell out several times. Failing of the RF during a run does not have a large effect. However, failing of POLIS can have a large influence on the polarisation. Since the polarisation is obtained by collecting data over a period of time in order to have enough statistics, a continuous change of the polarisation will result in an incorrect polarisation degree. If such a data point is analysed, and events measured with different polarisations are summed up, the resulting analysing power will be wrong. Therefore, it was necessary to cut out the time slices in these measurements, which were made during the failure of POLIS, and not to use them in the further analysis. The time information for these cuts was obtained from events recorded by the scaler units. An example is shown in figure 4.13. Determining the polarisation in a time slice for a certain data point is, in principle, possible. However, due to low statistics the uncertainty in the polarisation will be rather large. Since the polarisation turned out to be constant over time for most data points, the mean polarisation value, obtained by using a larger data set from the IBP

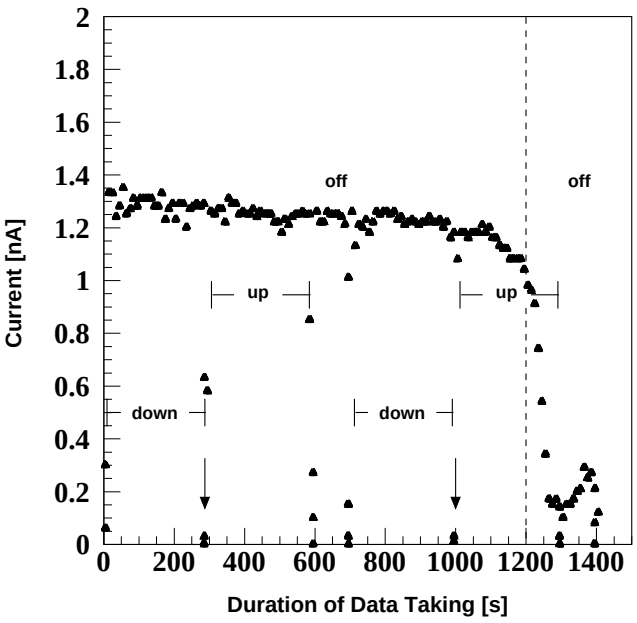

Figure 4.13: Cut on the global time. In this figure, the current is shown for the whole duration of the data taking for deuterons scattered to $\theta_{\mathrm{lab}} = 38^{\circ}$ at $E_p = 135$ MeV. By up, down *and* off*, the polarisation state of POLIS is depicted. Towards the end of the data taking, the current is decreasing rapidly, which is due to failing of POLIS. In the analysis of this run the last part where the current is decreasing, separated by a dashed line, was cut out. To distinguish from the ToF cut, this is referred to as a global time cut. When the state of POLIS is changed, e.g. at 300 s and 1000 s, marked by arrows, the current also drops shortly. However, during this time POLIS is not in a defined polarisation state and those events are, therefore, not taken into account during the analysis.*

measurements, could be used in the analysis of those data points.

Calculating and Cutting on the BBS Opening Angle

For the determination of the differential cross section, the solid angle had to be determined from the opening of the BBS. The analysing power is obtained from a ratio and does not depend directly on the solid angle. The solid angle can be determined from the target coordinates of the BBS, using the formulae given in appendix B. With these coordinates, it is then also possible to make smaller cuts on the BBS opening, and therefore also on the solid angle. The target coordinates are obtained from a ray-trace procedure using the focal-plane coordinates. To determine the transformation matrix needed for this procedure, a measurement was done using a sieve-slit aperture instead of the normal slit aperture at the BBS entrance. Since the positions of the holes in the sieve-slit are well known, positions measured at the focal plane can be correlated to holes in the sieve-slit at the BBS entrance, as is shown in figure 4.14. Using these correlations, a matrix can be fitted to obtain the BBS target coordinates from the observables in the focal plane.

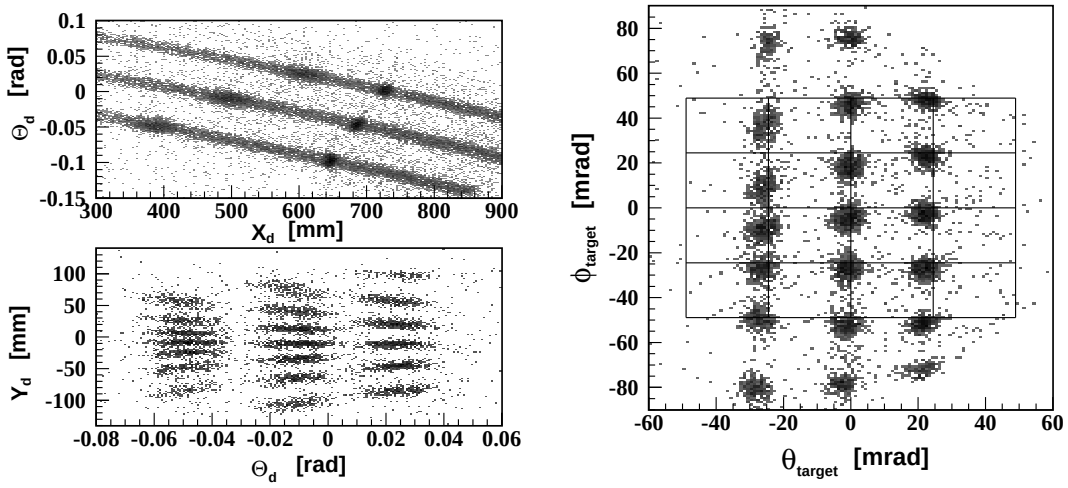

Figure 4.14: Sieve-slit measurement performed at 190 MeV beam energy at a laboratory scattering angle of $47°$. In the upper-left panel, a two-dimensional spectrum of the focal plane is shown. Two loci can be distinguished, both due to deuterons and protons emerging from the $^2\mathrm{H}(\vec{p}, dp)$ reaction. In the lower-left panel, the focal-plane coordinates Y_d versus θ_d are shown. Each of the points in this spectrum corresponds to one of the holes in the sieve-slit. On the right side, the target coordinates are shown. The grid shown in this picture depicts the actual positions of the holes in the sieve-slit aperture.

On the left side in figure 4.14, spectra measured at the focal plane when using a sieve-slit aperture at the entrance of the BBS are shown. On the right side, a two-dimensional spectrum of the reconstructed target coordinates is shown. The fit used for the spectrum shown on the right-hand side of figure 4.14 was used throughout the analysis of the data for the differential cross section. In figure 4.15, a spectrum of the BBS aperture and the results of the fitting procedure done for a measurement at 190 MeV are shown. As can be seen, the result of the fit for ϕ_{target} is far from satisfactory. Using these fits, it is not possible to obtain sensible spherical coordinates and therefore the correct solid angle. A slightly better fit was obtained by using a data base consisting of several measurements of the reactions $^{12}\mathrm{C}(p, p')^{12}\mathrm{C}$ and $^{11}\mathrm{B}(p, p')^{11}\mathrm{B}$ by the EuroSuperNova (ESN) collaboration, see e.g. [Han01]. The spectra obtained when using this fit were the ones shown in figure 4.14.

A further problem is a ϕ-dependent inefficiency of the ESN focal-plane detection system, which is not completely understood [Han01]. To account for both, the incorrect calculation of ϕ_{target} as well as the inefficiency of the ESN-detector, the normalisation factors obtained from elastic proton-proton scattering were used. These measurements will be explained in more detail in subsection 4.2.4. The solid angle was determined using the geometrical properties of the slit at the BBS entrance. In this case, the whole opening of the BBS entrance, corresponding to a solid angle of 7.8 msr, had to be used.

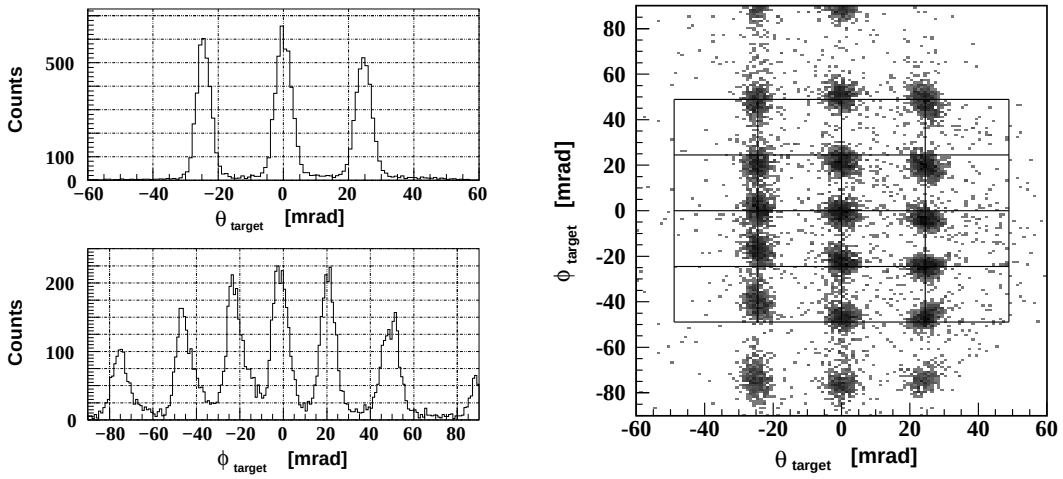

Figure 4.15: The target coordinates obtained from a fit of the focal-plane coordinates shown in figure 4.14. The coordinate θ_{target}, shown in the upper histogram on the left side, has been fitted with a second-order polynomial in X_d, Y_d and Θ_d. The peaks, corresponding to different holes in the sieve-slit, have a uniform width and give a similar distribution. In the lower histogram on the left side, the coordinate ϕ_{target} can be seen, obtained from a second-order polynomial fit in X_d and Y_d. As can be seen, the widths of the single peaks are not uniform and the distribution is rather broad. This leads to a distribution of ϕ_{target} which depends on θ_{target} as can be seen on the right side. Other polynomials up to fourth order in X_d, Y_d and Θ_d coordinates did not lead to better results.

4.2.3 Dead-time Corrections and Charge Collection

For a large vector analysing power, the number of events recorded by the data acquisition for a certain period of time could differ by a factor of two or more for different spin states, leading to spin-dependent dead-times. Therefore, the number of collected events had to be corrected for the dead-time for each spin state separately. In general, the dead-times in the cross-section measurements were kept below 20%. Here, the procedure of the analysis differs from the method employed by the ESN-collaboration. The normal way of correcting for dead-time is to sum up the number of events registered by scalers and, therefore, not suffering from computer dead-time, and those events recorded by the data acquisition. From these numbers, an averaged live-time is calculated by

$$\frac{\sum \text{recorded events}}{\sum \text{triggered events}} \tag{4.8}$$

at the end of the run. This approach assumes, that the beam parameters, like the polarisation and the beam current, stay constant during the whole run. As already remarked earlier, this is definitely not the case. Therefore, during the analysis, the number of events collected within ten seconds was corrected for the dead-time calculated from the scaler-events, which were recorded

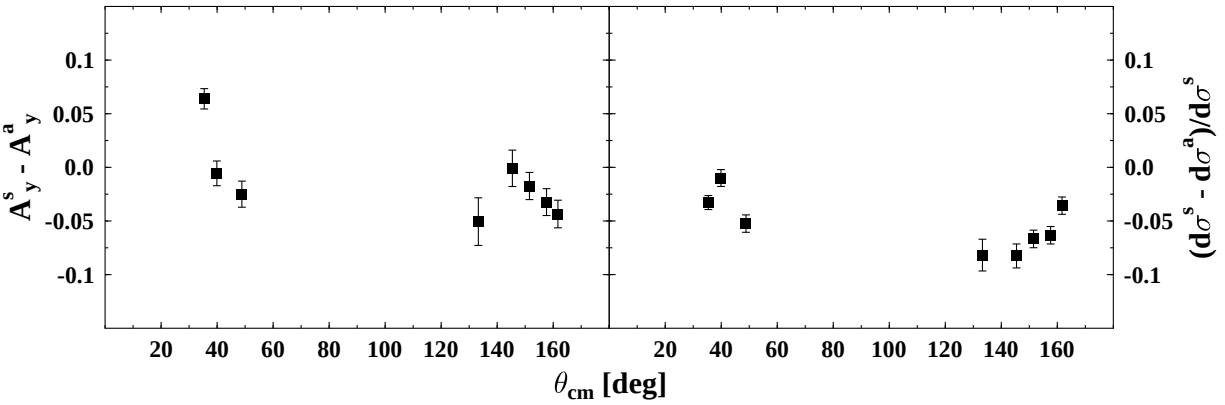

Figure 4.16: Shown is a comparison for different procedures of dead-time correction. On the left, the absolute difference between analysing powers obtained when using either of the two procedures for dead-time determination explained in the text is shown. On the right, the relative difference for the differential cross section is shown. Superscript 'a' denotes the average dead-time, superscript 's' the standard method employed throughout this work.

during the ten seconds of measurement. A comparison between the two different approaches is shown in figure 4.16. On the left side of figure 4.16, the absolute difference between analysing powers obtained when using an average dead-time (superscript *a*) and those obtained using the standard procedure (superscript *s*) of this work is shown. On the right of figure 4.16, the same is shown for the relative difference of the differential cross sections. As can be seen, the use of an averaged dead-time leads in certain cases to sizeable effects.

Also, the number of counted events had to be normalised to the collected charge for each spin state separately. In this case, however, the charge was summed up for each data point. The events were normalised to the charge when calculating the analysing power and the cross section.

4.2.4 Calculation of the Normalisation Factor and Efficiencies

To arrive at the final differential cross sections, corrections for effects which are common to protons and deuterons, such as the target thickness and the opening angle, have to be made. Furthermore, effects, which depend on the particle type, such as the VDC efficiency, have to be accounted for. These steps will be outlined in this subsection.

The Normalisation Factors

As was already remarked in section 3.6.1, the target thickness and other global properties of the BBS/ESN detection system, such as the beam intensity, were corrected for by using elastic proton-proton scattering. Since the observables of nucleon-nucleon scattering can be calculated rather precisely with modern nucleon-nucleon potentials, a precise overall normalisation factor can be obtained. Measurements of elastic proton-proton scattering were done at several angular

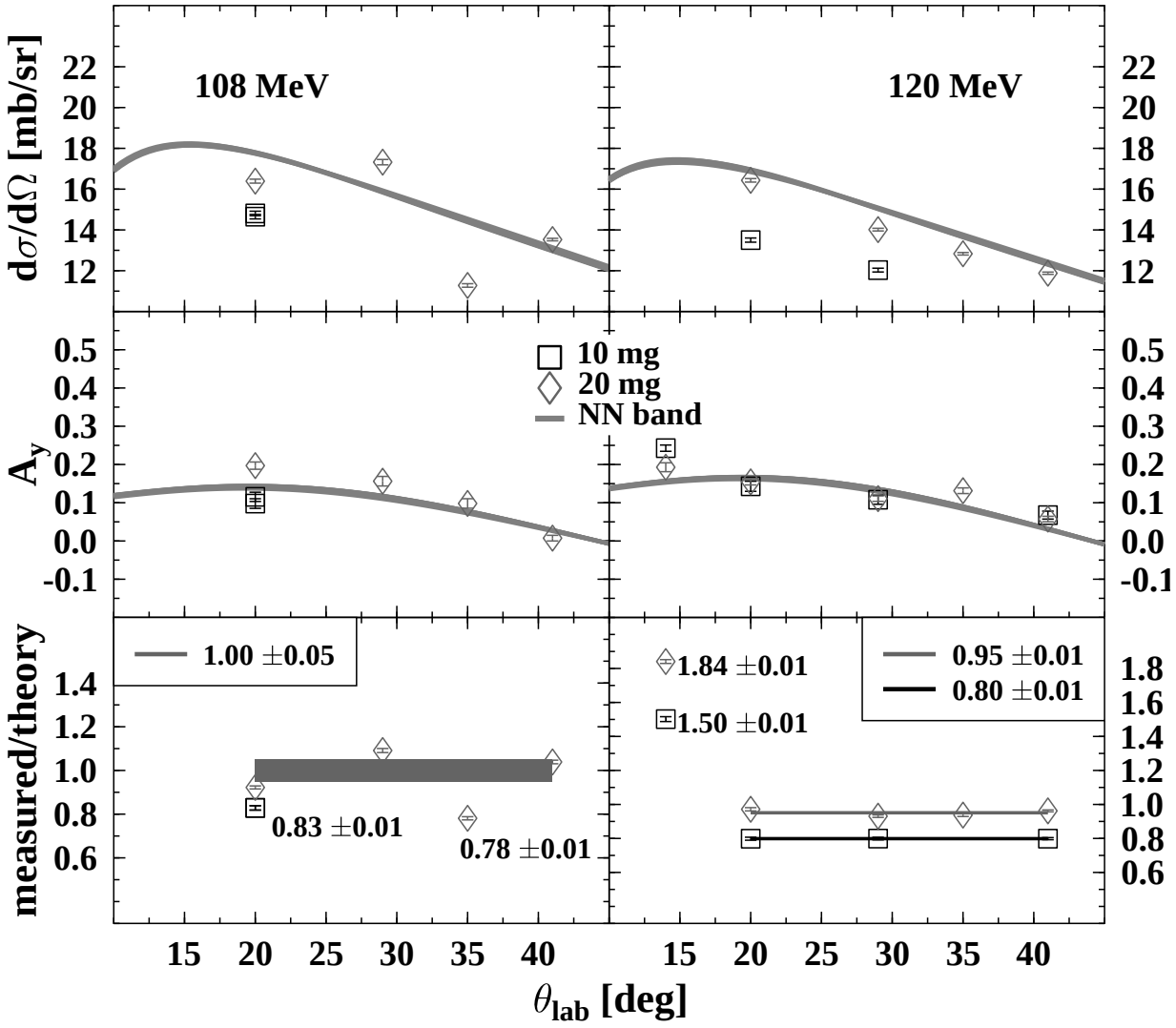

Figure 4.17: Results of the measurement of the proton-proton differential cross section and analysing power at 108 MeV on the left and 120 MeV on the right side for two different target thicknesses. Where averaging was possible, the weighted averages of the normalisation factors for the cross sections are shown as bands in lower panels.

settings for all beam energies during the cross-section measurements. In the cases, where polarised protons were used, the comparison of the measured proton-proton analysing power with the results obtained from the calculation also gave an indication of the accuracy of the determination of the degree of beam polarisation.

The analysis of the proton-proton scattering data was done in the same way and with the same analysis software as in the analysis of the proton-deuteron scattering data described in section 4.2. In figures 4.17-4.19, a comparison between the measured and the calculated differential

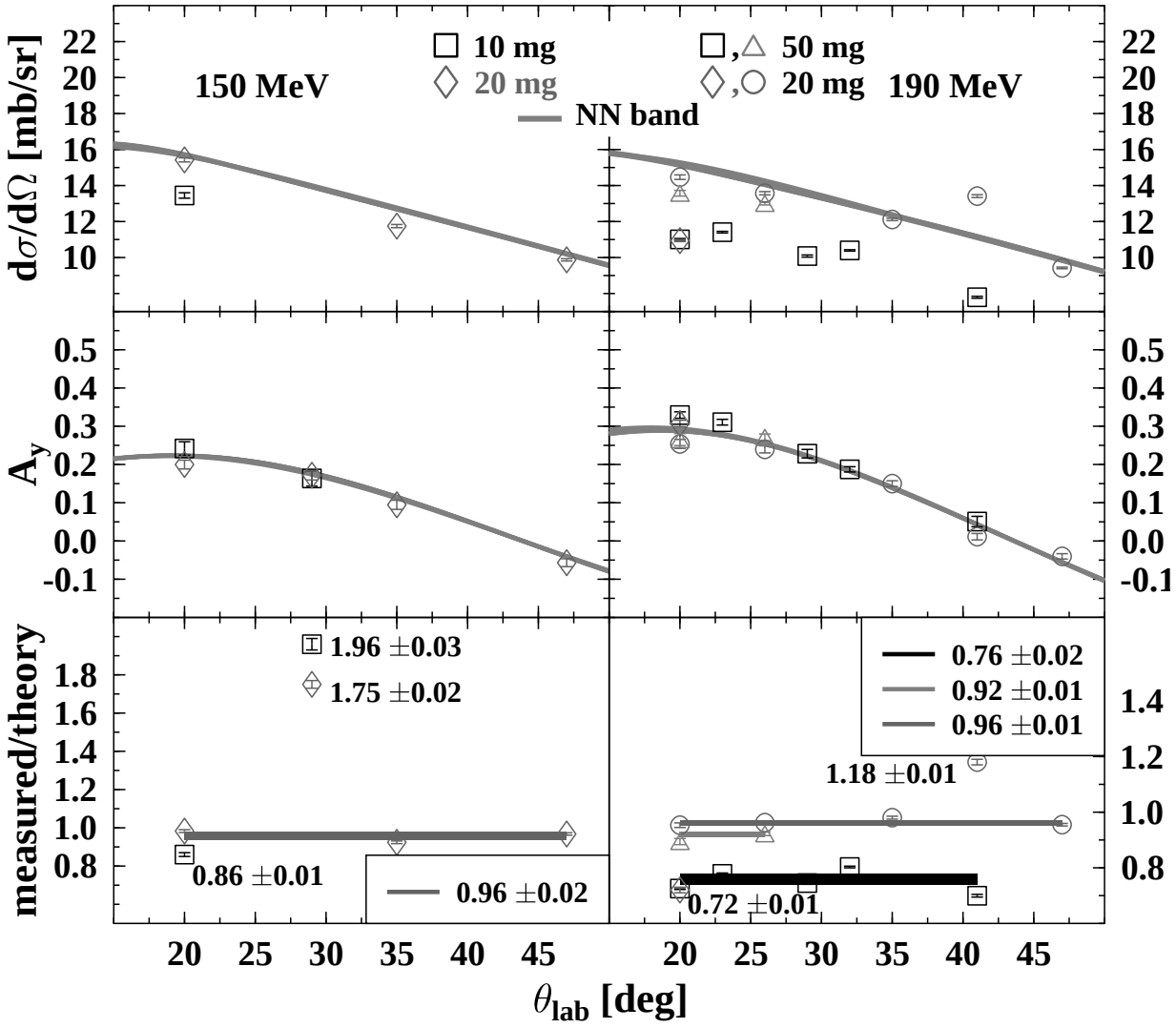

Figure 4.18: Same as figure 4.17 but for 150 and 190 MeV incident beam energies. At 190 MeV, the circles and triangles correspond to measurements done in April 2002.

cross sections and analysing powers, if polarised protons were used, and the ratio between measurements and calculations are shown. The theoretical calculation of the analysing power and the differential cross section is shown as a band, obtained from the potentials *Nijmegen I*, *Nijmegen II*, *Nijmegen 93* and *PWA 93* [Sto94, nno]. For further analysis, an average of the results of these four potentials was used, resulting also in a theoretical uncertainty. This uncertainty was propagated in the uncertainty of the normalisation factors.

At bombarding energies of 108, 150 and 190 MeV, as can be observed in figures 4.17 and 4.18, the measured differential cross section shows a deviation from theory which depends on the scattering angle. A possible explanation could be that the beam spot on the target drifted

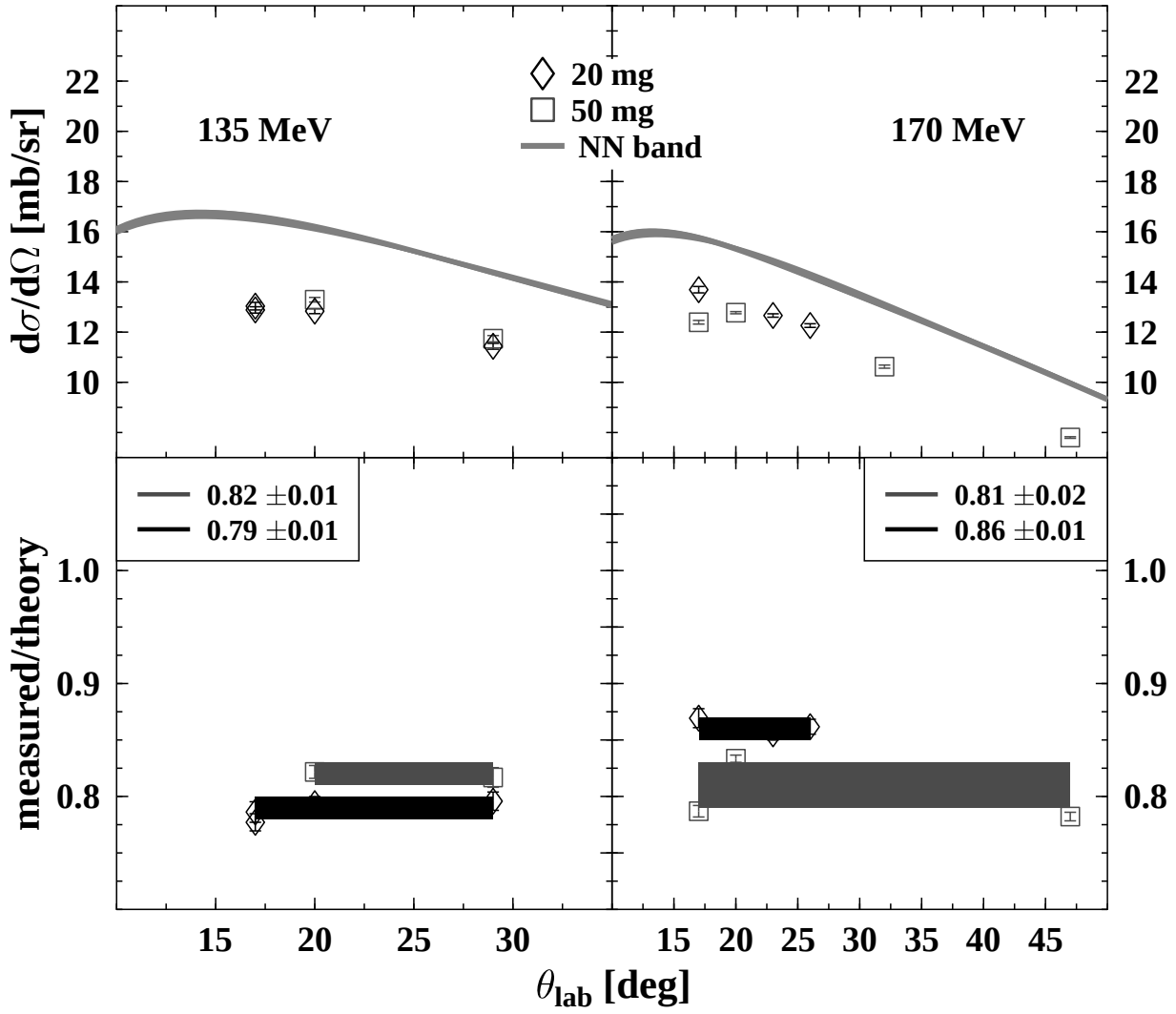

Figure 4.19: Same as figure 4.17 but for 135 and 170 MeV incident beam energies. These measurements were done with an unpolarised beam from CUSP and no analysing powers were measured.

slightly during the experiment. Since the targets do not have a uniform thickness across their surfaces, as was explained in section 3.6, this would lead to a different target thickness and therefore to a different normalisation factor. Another possible explanation could be the melting of the polyethylene target during the experiment. However, measurements done at later times do not show a constant change of the normalisation factor, and this explanation seems therefore rather unlikely. Therefore, at these three energies, an overall normalisation factor was obtained from the weighted averages except for those scattering angles, where the normalisation factor shows a sizeable deviation.

Furthermore, at 120 MeV, as can be seen in figure 4.17, the normalisation factors measured at 14° differ from the ones measured at larger angles. Since at laboratory scattering angles $8.5^\circ \leq \theta_{\mathrm{lab}} \leq 14^\circ$ a Faraday cup inside the BBS was used, the deviation is probably due to a misalignment of the Faraday cup. Therefore, for scattering angles $8.5^\circ \leq \theta_{\mathrm{lab}} \leq 14^\circ$, the normalisation factor obtained from a measurement at $\theta_{\mathrm{lab}} = 14^\circ$ was used. For $\theta_{\mathrm{lab}} \geq 20^\circ$ at 120 MeV, an overall normalisation factor obtained from the weighted averages of the individual measurements was used. Since the cross-section measurements at 108 and 150 MeV were done during the same experiment as 120 MeV, also here the normalisation factor obtained for $\theta_{\mathrm{lab}} = 14^\circ$ at 120 MeV had to be applied to those measurements that were done at $8.5^\circ \leq \theta_{\mathrm{lab}} \leq 14^\circ$.

At 170 MeV, an overall normalisation factor could be obtained from the weighted averages of the individual measurements for both targets. At 190 MeV, overall normalisation factors were obtained for the target with 50 mg/cm^2. From the measurements done with the 20 mg/cm^2 target in April 2002, an overall normalisation factor was obtained except for the measurements around 41°, where a large deviation can be observed in figure 4.18.

Another factor, that should be taken into account is radiation damage to the target. In the case of C_2H_4-C_2D_4 targets, radiation damage would induce a breaking of the C-C bonding, leading to a loss of hydrogen and deuterium. Also, it is known that the radiation damage depends on the manufacturing process of the target. Nevertheless, some estimate can be made based on known numbers. Since, to a good approximation, the effect should be the same for hydrogen and deuterium, the ratio between both contents should not change significantly and the effect on the normalised differential cross section should be small. This assumption was confirmed by mass-spectroscopic measurements of the ratio which were done after the experiments had been performed [Kui02, Mei02]. These measurements showed that the C_2D_4:C_2H_4 ratios in irradiated and not-irradiated regions of the target did not differ. Using an estimation of $\approx 1\%$ loss of deuterium per 10^7 Gy radiation dose [Hin02], an estimation for the possible radiation damage can be made. The average energy deposit for an incident-beam energy of 108 MeV is ≈ 13 MeV/(proton·g/cm^2). For a beam area of roughly 5 mm^2, a current of 1 nA and a radiation time of 24 h $\approx 10^5$ s, the deposited radiation would be $\approx 10^7$ Gy, i.e., a decrease of the hydrogen and deuterium content of $\approx 1\%$. This estimation is only true for the lowest beam energy used in this work; at higher bombarding energies, the deposited energy would be even less. Furthermore, the total systematic uncertainties of the differential cross sections, which will be discussed in section 4.2.6 are about 5%; a 1% effect could, therefore, not be observed. As can be seen in figures 4.17-4.18, the normalisation factors obtained from elastic proton-proton scattering are rather constant, leading to the conclusion that radiation damage is negligible for the measurements done in this work.

The measured analysing powers would not suffer from either of the afore-mentioned effects. As can be seen in figures 4.17-4.18, this is also not the case and the measured analysing powers agree well with the band obtained from theory. The normalisation factors which were used in the final analysis can be found in table 3.2 on page 47.

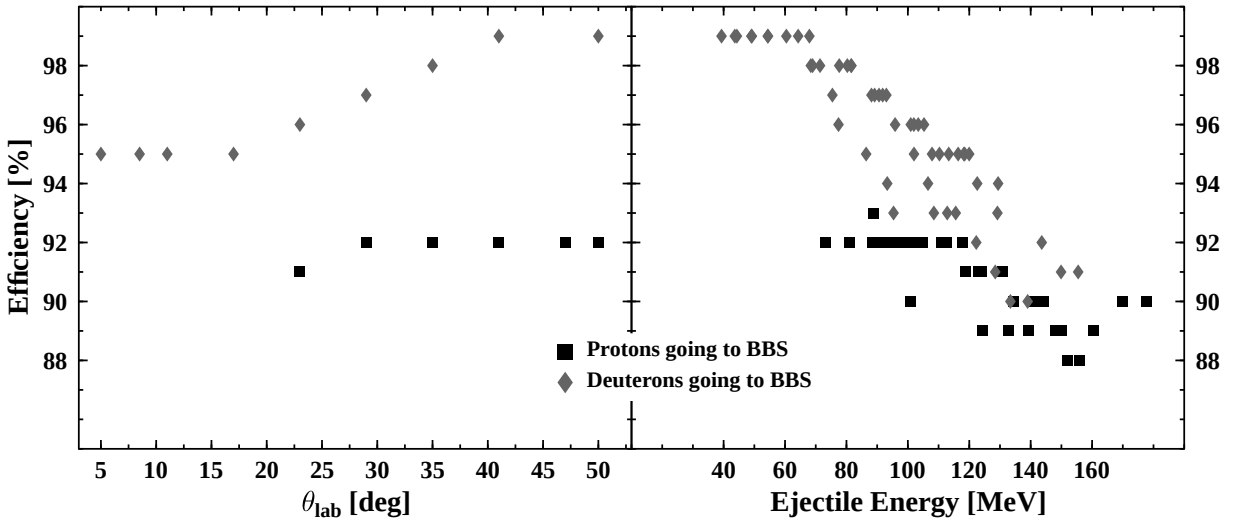

Figure 4.20: Efficiency of the vertical-drift chamber for each particle type as a function of the scattering angle (on the left) and the ejectile energy (on the right). The beam energy was 135 MeV for the left panel while all beam energies were used in producing the right figure. The diamonds correspond to outgoing deuterons, the squares to outgoing protons. The uncertainty for each data point was estimated to be $\approx 1\%$.

Vertical Drift Chamber Efficiency

Apart from global corrections, such as the correction for the target thickness and the beam current, which could be accounted for by using the elastic proton-proton differential cross section, as described in the last subsection, efficiencies of the detection system depending on the particle-type of the ejectile had to be corrected for separately. This concerned mainly the efficiency of the VDC detection and the VDC reconstruction with respect to protons and deuterons.

The efficiency $\epsilon_i (i = 1 \ldots 4)$ of one plane of the VDCs was determined as

$$\epsilon_i = \frac{\sum \text{ one hit in all four planes}}{\sum \text{ one hit in three planes}} \tag{4.9}$$

The total efficiency of the VDC was calculated from the product of the efficiencies of all four planes,

$$\epsilon_{\mathrm{VDC}} = \prod_{i=1}^{4} \epsilon_i. \tag{4.10}$$

This efficiency contained the convolution of the detection efficiency and the efficiency of the reconstruction algorithm used to determine the interception point in the plane from the drift times.

The efficiency obtained from formulae (4.9) and (4.10) turned out to depend on the type of particle traversing the drift chamber, as is shown in figure 4.20. As can be seen, the efficiency of

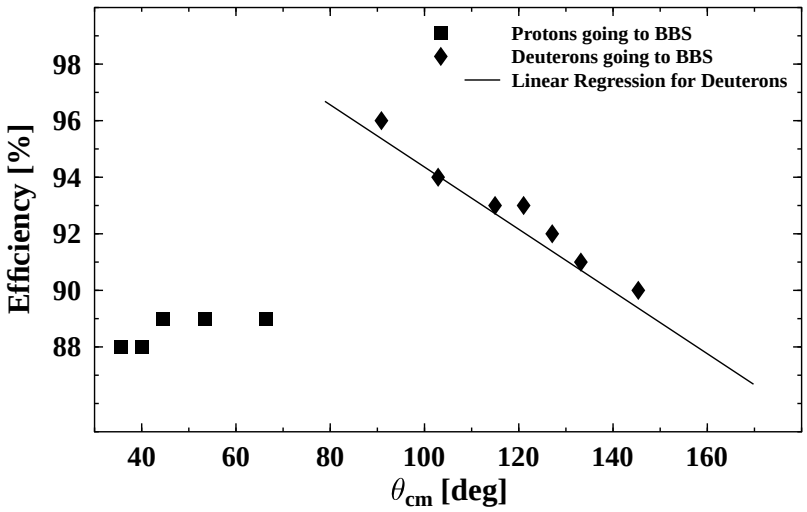

Figure 4.21: Efficiency as a function of θ_{cm} for 170 MeV incident-beam energy. The efficiency for detecting protons is rather constant within an uncertainty of 1%, whereas that for the deuterons shows a dependence on θ_{cm} which has been fitted with a linear regression.

the protons is rather constant within 1% over the angular range where measurements were done and for each incident-beam energy. Therefore, the differential cross section was corrected using a common efficiency for each incident-beam energy at those points, where the outgoing proton was detected. Another example for the efficiency of the protons at 170 MeV incident-beam energy as a function of θ_{cm} can be seen in figure 4.21.

For the deuterons, the efficiency shows a dependence on the ejectile energy, which corresponds to a dependence on the centre-of-mass scattering angle. In figure 4.21, the efficiency is shown as a function of θ_{cm} for an incident-beam energy of 170 MeV. The dependence of the efficiency on θ_{cm} can be approximated by a linear regression. This was also the case for the measurements at the other beam energies and, therefore, the VDC efficiency for deuterons was calculated as a linear function of θ_{cm}. This was done separately for each beam energy.

4.2.5 Calculation of A_y and the Differential Cross Section

In this subsection, the formalism for calculating the differential cross section and the vector analysing power for measurements done with a polarised beam is briefly reviewed. For measurements done with an unpolarised beam from the CUSP source, the formulae given in equations (4.11) and (D.3) in appendix D can, of course, be applied directly.

When the events for a data point were selected according to the cuts described in section 4.2 and corrected for dead-time, the spin-dependent differential cross section was calculated for each

spin state according to the formula derived in appendix D

$$\begin{aligned}\frac{d\sigma^s}{d\Omega}\left[\frac{\mathrm{mb}}{\mathrm{sr}}\right] = & \frac{1}{3.75872\,[\mathrm{cm}^2/(\mathrm{mb}\cdot\mathrm{C}\cdot\mathrm{mol})]}\times \\ & \frac{m^{\mathrm{mol}}_{\mathrm{target}}[\mathrm{mg/mol}]}{n_{\mathrm{atoms}}}\cdot\frac{Z[\mathrm{C}]\cdot N_{\mathrm{collected}}}{Q}\times \\ & \left(\frac{\delta x\,[\mathrm{mg/cm}^2]}{\cos\delta_{\mathrm{target}}}\right)^{-1}\cdot\frac{1}{\Delta\Omega[\mathrm{msr}]}\cdot\frac{1}{\epsilon_{\mathrm{pp}}\cdot\epsilon_{\mathrm{VDC}}}\end{aligned} \tag{4.11}$$

where $N_{\mathrm{collected}}$ is the number of dead-time-corrected collected events, Q is the collected charge, Z is the charge of the projectile, $m^{\mathrm{mol}}_{\mathrm{target}}$ is the target mass in atomic units, n_{atoms} is the number of atoms in the compound molecule, δx is the target thickness, δ_{target} is the angle between the normal to the target and the beam direction and $\Delta\Omega$ is the solid angle. ϵ_{pp} is the correction factor obtained from elastic proton-proton scattering and ϵ_{VDC} the efficiency of the vertical drift chamber.

The relation between the spin-dependent cross section $d\sigma^s$ and spin-averaged cross section $d\sigma^0$ is

$$d\sigma^s = d\sigma^0(1 + p^s \cdot A_y \cdot \cos\phi) \tag{4.12}$$

for a vector polarisation p^s and vector analysing power A_y. ϕ is the angle between the direction of polarisation and the normal to the scattering plane in the laboratory frame of reference. The definition in the literature [Ohl72] is that for an incoming proton with spin up, $\phi = 0^\circ$ corresponds to the scattering of the outgoing proton to the *left* and $\phi = 180^\circ$ to the *right*. For a setting, where the BBS selects the outgoing deuterons and the outgoing protons are measured by the coincidence scintillator, the relation between $d\sigma^s = d\sigma^\uparrow$ and $d\sigma^0$ would be

$$d\sigma^\uparrow = d\sigma^0(1 + p^\uparrow \cdot A_y) \tag{4.13}$$

for an incoming proton with spin up. If the incoming proton had spin down, the angle ϕ would be shifted by 180°. For the case mentioned here, the scattered proton would see the coincidence scintillator at an angle $\phi = 180^\circ$ and the relation between $d\sigma^s = d\sigma^\downarrow$ and $d\sigma^0$ would then be

$$d\sigma^\downarrow = d\sigma^0(1 - p^\downarrow \cdot A_y). \tag{4.14}$$

Since for the measurement with the BBS, the acceptance of the BBS at the angles measured is sufficiently small and only the possibilities for $\phi = 0^\circ$ and $\phi = 180^\circ$ exist, the minus sign in equation (4.14) could also be absorbed in the polarisation, assigning a negative polarisation value to the down polarisation. In this case, equations (4.13) and (4.14) look alike.

From the two cross sections $d\sigma^\uparrow$ and $d\sigma^\downarrow$ with the polarisation $p^\uparrow$ and $p^\downarrow$, where $p^\downarrow < 0$, the analysing power can be calculated,

$$A_y = \frac{d\sigma^\uparrow - d\sigma^\downarrow}{p^\uparrow d\sigma^\downarrow - p^\downarrow d\sigma^\uparrow}. \tag{4.15}$$

Equation (4.15) holds for any polarisation degree, provided that care is taken with the sign of the polarisation.

For settings, where the outgoing protons are selected by the BBS and the outgoing deuterons are measured with the coincidence scintillator, care has to be taken. For an incoming beam with polarisation up, the outgoing protons are scattered to the *right*, i.e., $\phi = 180°$, and the vector analysing power calculated from equation (4.15) has to multiplied by -1.

Once the vector analysing power has been calculated, equation (4.13) or (4.14) may be used to calculate the spin-averaged differential cross section $d\sigma^0$,

$$\begin{aligned} d\sigma^0 &= \frac{d\sigma^s}{1 + p^s A_y} \\ &= \frac{p^\uparrow d\sigma^\downarrow - p^\downarrow d\sigma^\uparrow}{p^\uparrow - p^\downarrow} \end{aligned} \tag{4.16}$$

where the polarisation p^s can be larger or smaller than zero. Even though the efficiencies are included in the calculation of the cross section, they may be by-passed if the interest lies only in the analysing powers. These depend only on the ratio of the cross sections and the efficiencies cancel each other. This assumes, of course, that the efficiencies are independent of the spin as was the case for the measurements done in this work.

4.2.6 Propagation of the Uncertainties

In the following, the uncertainties of the measurements of the reaction $^2\mathrm{H}(\vec{p}, dp)$ will be discussed. For the calculation of all uncertainties, the propagation formula [Bev92]

$$\left(\delta f(x_i)\right)^2 = \sum_i \left(\frac{\partial f(x_i)}{\partial x_i} \Delta x_i \right)^2 \tag{4.17}$$

has been employed. In some cases, also the correlation terms Δx_{ij} had to be taken into account.

Uncertainty Propagation in the Differential Cross Section

For the sake of simplicity, the abbreviation

$$d\sigma \equiv \frac{d\sigma}{d\Omega} \tag{4.18}$$

will be used in this subsection. The statistical uncertainty in the differential cross section is given by the statistical uncertainty in the number of counted events, i.e.,

$$\Delta d\sigma_{\mathrm{stat}} = \frac{1}{3.75872} \cdot \frac{m^{\mathrm{mol}}_{\mathrm{target}}}{n_{\mathrm{atoms}}} \cdot \frac{Z \cdot \sqrt{N_{\mathrm{collected}}}}{Q \cdot \delta_{\mathrm{target}}} \cdot \frac{1}{\Delta\Omega} \tag{4.19}$$

However, when polarised protons were used and the cross section was determined from formula (4.16), the statistical uncertainty of the spin-averaged differential cross section has to be determined by

$$\Delta d\sigma^0_{\mathrm{stat}} = \frac{1}{\sqrt{(p^\uparrow - p^\downarrow)^2}} \sqrt{(p^\downarrow \Delta d\sigma^\uparrow)^2 + (p^\uparrow \Delta d\sigma^\downarrow)^2}, \tag{4.20}$$

which is obtained from applying the propagation formula (4.17) to equation (4.16). The uncertainties of the spin-dependent cross sections are given by (4.19). In this case, also the uncertainty due to the polarisation has to be taken into account. The systematic uncertainty in the differential cross section, which is due to the uncertainty in the polarisation, is

$$\Delta d\sigma^p_{\mathrm{sys}} = \frac{\sqrt{(d\sigma^\uparrow - d\sigma^\downarrow)^2}}{(p^\uparrow - p^\downarrow)^2} \sqrt{(p^\downarrow \Delta p^\uparrow)^2 + (p^\uparrow \Delta p^\downarrow)^2 - 2p^\uparrow p^\downarrow \Delta p^{(\uparrow\downarrow)}} \tag{4.21}$$

In equation (4.21), $\Delta p^{(\uparrow\downarrow)}$ is the error-correlation matrix. Since ions with spin up and spin down are produced in the same source, possible correlation effects have to be taken into account. Equation (4.21) takes on its largest value, when both spin values are completely anti-correlated. In that case, using the notation $p^\uparrow > 0,\ p^\downarrow < 0$, the correlation matrix is

$$\Delta p^{(\uparrow\downarrow)} = -(\Delta p^\uparrow) \cdot (-\Delta p^\downarrow). \tag{4.22}$$

Assuming $\Delta p^\uparrow = \Delta p^\downarrow \equiv \Delta p$, which was the case during most of the measurements done in this work, equation (4.21) reduces to

$$\frac{\Delta d\sigma^p_{\mathrm{sys}}}{d\sigma^0} = A_y \Delta p. \tag{4.23}$$

Equation (4.23) gives an idea of the influence of the polarisation uncertainty on the uncertainty in the differential cross section. However, in the final error analysis equations (4.21) and (4.22) were utilised.

Uncertainties in the other variables contained in equation (4.11) will lead to systematic uncertainties. Variables which will lead to systematic uncertainties are the luminosity, i.e. target thickness and the collected charge, the opening angle and the VDC efficiency. Since the nominal luminosity was used and corrected for by using the normalisation factor obtained from proton-proton scattering, the uncertainty of the luminosity is given by the uncertainty of ϵ_{pp}. The same holds for the uncertainty in the solid angle. The total contribution of these uncertainties to the uncertainty in the differential cross section is given by

$$\left.\frac{\Delta d\sigma}{d\sigma}\right|_{\mathrm{sys}} = \sqrt{\left(\frac{\Delta \epsilon_{pp}}{\epsilon_{pp}}\right)^2 + \left(\frac{\Delta \epsilon_{\mathrm{VDC}}}{\epsilon_{\mathrm{VDC}}}\right)^2} \tag{4.24}$$

which is obtained by applying (4.17) to (4.11). The uncertainty for the efficiency correction was estimated to $\approx 1\%$. This estimate is based on the efficiency analysis. For the uncertainty of the solid angle, an upper estimation of $\approx 1\%$ was made, which is already included in $\Delta\epsilon_{pp}$. The uncertainties in the correction factor are given in table 3.2 on page 47. A summary of all the uncertainties is given in table 4.2.

Table 4.2: Uncertainties in $d\sigma/d\Omega$ and A_y. The actual uncertainties for each incident-beam energy are given in tables G.1-G.8 in appendix G.

Uncertainty Source	*Uncertainty*
Differential Cross Section:	
statistical uncertainty	$< 2\%$
systematical uncertainties:	
1) polarisation	*in general* $\lesssim 1\%$, $\lesssim 3\%$ *at 120 MeV*
2) normalisation	*in general* $\lesssim 2\%$, $\approx 5\%$ *for few exceptions*
3) efficiency	$\approx 1\%$
4) $\Delta\Omega$	*contained in 2)*
5) point-to-point uncertainty	$\lesssim 5\%$, *contained partially in 2)*
$\sqrt{\sum (\textit{systematic uncertainties})^2}$	*in general* $< 6\%$, *at most* 7%
Analysing Power:	
statistical uncertainty	$\lesssim 0.01$
systematical uncertainties:	
polarisation	*in general* $\lesssim 3\%$, $\lesssim 8\%$ *at 120 MeV*

Uncertainty Propagation in the Analysing Power

The statistical uncertainty in the analysing power was obtained by applying the formula (4.17) to equation (4.15),

$$\Delta A_y|_{\text{stat}} = \frac{\sqrt{(p^\uparrow - p^\downarrow)^2}}{(p^\uparrow d\sigma^\downarrow - p^\downarrow d\sigma^\uparrow)^2} \sqrt{(d\sigma^\downarrow \Delta\sigma^\uparrow)^2 + (d\sigma^\uparrow \Delta\sigma^\downarrow)^2}. \tag{4.25}$$

Equation (4.25) contains only the statistical uncertainties due to the spin-dependent cross sections $d\sigma^\uparrow$ and $d\sigma^\downarrow$, and not the uncertainties from the polarisation measurements. For a given polarisation, determined by the IBP measurement, the uncertainty in the polarisation degree of the proton, independent of its systematic or statistical origin, will result in a systematic uncertainty in the measured vector analysing power. The systematic error of the analysing power, which is due to the uncertainty in the polarisation degree, is given by

$$\Delta A_y|_{\text{sys}} = \frac{d\sigma^\uparrow - d\sigma^\downarrow}{(p^\uparrow d\sigma^\downarrow - p^\downarrow d\sigma^\uparrow)^2} \sqrt{(d\sigma^\downarrow \Delta p^\uparrow)^2 + (d\sigma^\uparrow \Delta p^\downarrow)^2 - 2\Delta p^{(\uparrow\downarrow)} d\sigma^\uparrow d\sigma^\downarrow}. \tag{4.26}$$

In contrast to equation (4.21), the systematic uncertainty in the analysing power takes on its largest value, when the uncertainties in the polarisation are completely correlated. Although this is not consistent with the assumption made for equation (4.22), it is an upper estimation of the uncertainty in the analysing power. The error correlation matrix is then

$$\Delta p^{(\uparrow\downarrow)} = \Delta p^\uparrow \cdot (-\Delta p^\downarrow), \tag{4.27}$$

which is due to the notation $p^\uparrow > 0, p^\downarrow < 0$. In this case, if $\Delta p^\downarrow = \Delta p^\uparrow \equiv \Delta p$ and $-p^\downarrow = p^\uparrow \equiv p$,

$$\frac{\delta A_{y,\text{sys}}}{A_y} = \frac{\Delta p}{p}. \tag{4.28}$$

In the analysis of the data, equations (4.26) and (4.27) were used for the final error analysis.

4.3 Analysis of the SALAD Data

In this section, the analysis of the data taken during the measurement of the $\mathrm{H}(\vec{d}, dp)$ reaction at $E_d = 130$ MeV with SALAD will be described. This experiment was considered to be a feasibility test, as the polarisation of the beam could not be obtained during the measurements. For future experiments, using SALAD in a modified form including a new polarimeter, the polarisation will be determined with a lamb-shift polarimeter in the low-energy beam line. Then, the vector- and tensor-analysing powers of the elastic scattering channel will be measured.

4.3.1 Track Reconstruction and Event Selection

The general procedure for analysing the data was to build for each event a track through SALAD starting with the MWPC. Therefore, it was tried to correspond a valid hit in the MWPC with a hit in the ΔE and the energy detectors. The final track was then obtained after particle identification. However, no events were thrown away if no correspondence between a valid hit in the MWPC and a hit in the ΔE-E hodoscope could be obtained, accounting for the possibility of good events which did not reach the energy detector due to the low energy of the emerging particles. Due to the kinematics, deuterons with kinetic energies below a certain threshold stop in the ΔE detector. For these events, the corresponding proton, which is also scattered to a forward angle, causes a trigger in the energy scintillator. The MWPC, which is positioned upstream of the ΔE detector, records two tracks. However, the analysis of two events based solely on the MWPC tracks proved not to be reliable due to insufficient energy information.

The start of the tracking algorithm was the correspondence check of the MWPC. The correspondence check was done by taking hits in the x and y plane and corresponding them with a hit in the u plane. The procedure for this correspondence check has been used in earlier experiments with SALAD and is described in detail in references [Vol99, Hui99, Mes99, Vol01]. Hits in the x and y plane, which could not be corresponded to a hit in the u plane, were thrown away. These events were later corrected for by the efficiency of the MWPC. From the crossing point of a particle through the MWPC, its polar and azimuthal scattering angles were obtained.

With the events which had survived the MWPC analysis, a correspondence check with the energy and the ΔE detectors was made, using the MWPC x and y information for the correspondence with the ΔE detector and the θ and ϕ information for the correspondence with the energy detector. As mentioned earlier, no event was discarded if no energy or ΔE detector could be corresponded. The information obtained in this way was, however, used in a later stage of the data analysis.

In the upper-left panel of figure 4.22, a two-dimensional plot of the position in the x and y planes of the MWPC is shown after the correspondence check with the scintillators has been performed. In the upper-right panel of this figure, the two-dimensional plot of the y and x wires of the MWPC is shown for deuterons crossing the MWPC. This spectrum was projected after the final tracking and particle identification through SALAD, which will be described later in more detail, had been done. The dark outer ring that can be observed in both spectra corresponds to a scattering angle of $\approx 30^\circ$, where both deuterons and protons originating from the same reaction are scattered to a similar polar angle. A small number of artificial hits in the middle stem from a

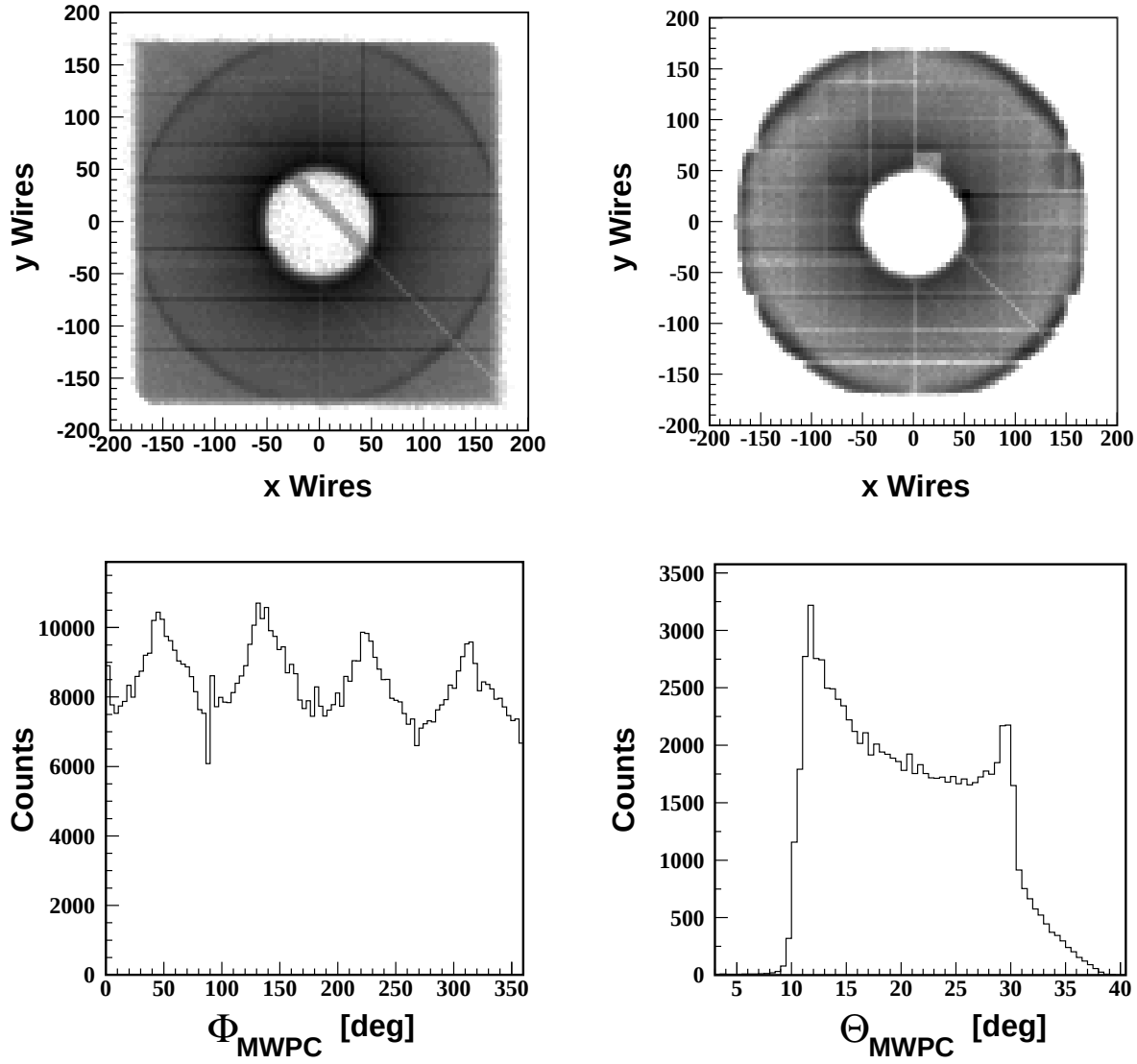

Figure 4.22: Spectra generated from MWPC information are shown. In the upper left panel, a two-dimensional plot of hits in the MWPC is shown after the correspondence check between x, y and u planes was done. The 'artificial' hits in the middle stem from a noisy wire in the u plane. However, it should be noted that the spectrum is shown with a logarithmic scale in the z-direction. On the upper right side, the same plot is shown for deuterons crossing the MWPC, after the final tracking and particle identification through SALAD has been done. In the lower left panel, the range of the azimuthal scattering angle ϕ is depicted, and in the right panel, the polar scattering angle θ.

noisy wire in the u plane. In the lower panels of figure 4.22, the range of the azimuthal scattering angle ϕ and the polar scattering angle θ are depicted on the left and right, respectively. Also in

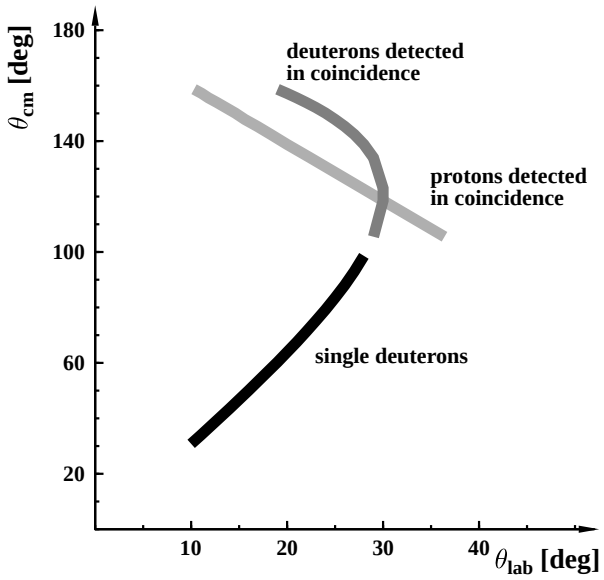

Figure 4.23: Schematic drawing of the angular range covered by SALAD. The energy-threshold for the deuterons, which has not been considered here, will lead to a cut-off at $\theta_{\mathrm{cm}} \approx 145°$.

this picture, a peak can be observed at $\theta \approx 30°$.

Further analysis relied on the kinematics of the energy and scattering angle for elastic deuteron-proton scattering with an incoming deuteron, which is described by

$$E'_d = \frac{1}{E_{\mathrm{tot}}^2 - p_d^2 \cos^2\theta_d} \left\{ E_{\mathrm{tot}}(E_d m_p + m_d^2) \pm m_p p_d^2 \cos\theta_d \sqrt{1 - \left(\frac{m_d}{m_p}\sin\theta_d\right)^2} \right\} \qquad (4.29)$$

and

$$\cos\theta_{\mathrm{cm}} = 1 + \frac{E_{\mathrm{tot}}^2 - p_d^2}{m_p p_d^2}[E'_d - E_d]. \qquad (4.30)$$

Formulae (4.29) and (4.30) give the relativistic energy E'_d of an elastically-scattered deuteron and its centre-of-mass scattering angle θ_{cm} as a function of the laboratory scattering angle θ_d. m_d and m_p are the deuteron and proton masses, $E_d = \gamma m_d$ is the relativistic energy of the incoming deuteron, p_d the corresponding momentum and $E_{\mathrm{tot}} = E_d + m_p$ the total energy of the system (assuming the proton to be initially at rest). A derivation of formulae (4.29) and (4.30) is given in appendix E. As can be seen, two possible signs are present before the square root in formula (4.29). If the mass of the incoming particle is smaller than the mass of the target particle, only the '$+$' sign is of relevance. However, if the mass of the incoming particle is larger than the mass of the target particle (as in the present case), the square root itself will become zero at a certain laboratory scattering angle and after this point, the '$-$' sign solution has to be applied with the

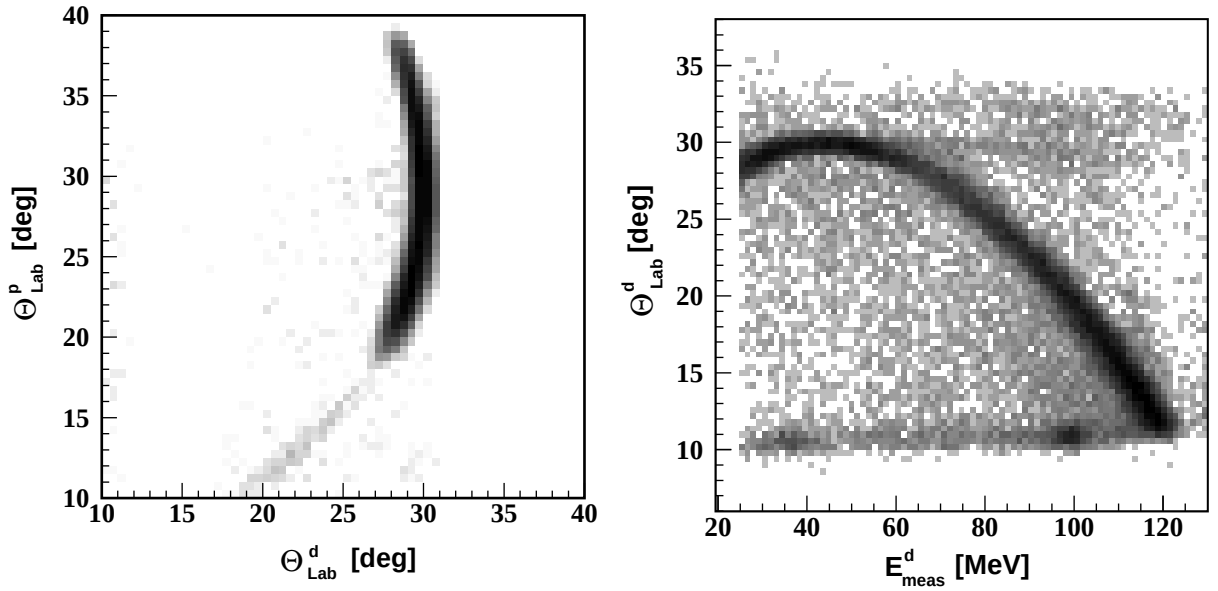

Figure 4.24: Shown are the kinematical limits of the events detected by SALAD. On the left, the laboratory scattering angle of protons is plotted versus the laboratory scattering angle of deuterons for particles emerging from the reaction $\mathrm{H}(\vec{d}, dp)$ *and detected in coincidence by SALAD. On the right side, the scattering angle of the deuteron is plotted against its measured energy for coincidence and single-track events. The turning point of the deuterons is located at an energy of* ≈ 44 *MeV. Further information is given in the text.*

scattering angle θ_d going back to $0°$. The laboratory scattering angle, at which

$$1 - \left(\frac{m_d}{m_p}\sin\theta_d\right)^2 = 0 \tag{4.31}$$

depends only on the mass ratio of the two particles and is $\theta_{\mathrm{lab}} = 30.02°$ for the case of the reaction $\mathrm{H}(\vec{d}, dp)$. Therefore, the deuterons will never be scattered to laboratory angles larger than about $30°$. Deuterons with the higher energy, i.e., the kinetic energy obtained when using the '$+$' sign in equation (4.29), will be detected ideally as pure single hits, since the corresponding protons fall outside the acceptance of SALAD. Deuterons with the lower energy, corresponding to the '$-$' sign in formula (4.29), will be detected simultaneously with the corresponding proton. Below a scattering angle of $\theta_{\mathrm{d}} \approx 26°$, the kinetic energy of the deuteron of the '$-$' sign solution is not sufficient to reach the energy detector and cause a trigger. However, the event, triggered by a proton in the energy detector, has two tracks in the MWPC. A scheme of the centre-of-mass angles versus laboratory angles, at which protons and deuterons are detected in SALAD is shown in figure 4.23. In this schematical drawing, the energy-threshold for the deuterons has not been considered. The kinematics described so far are also shown in figure 4.24. On the left side of figure 4.24, the laboratory scattering angle of protons is plotted versus the one of deuterons for particles emerging from the reaction $\mathrm{H}(\vec{d}, dp)$ and detected in coincidence in SALAD. While

the protons are scattered to angles between $20^\circ \lesssim \theta_{\mathrm{prot}} \lesssim 40^\circ$, the deuterons are scattered to laboratory angles $\lesssim 30^\circ$ but are detected only beyond $\approx 26^\circ$ due to the energy threshold imposed by the ΔE detector. On the right side, the scattering angle of the deuteron is plotted against its measured energy for coincidence and single-track events. Also here, it can be seen that the maximum scattering angle for deuterons is about 30° at an energy of ≈ 44 MeV.

For the event selection, use of the ΔE-E information was made. In figure 4.25, spectra of the ΔE-E hodoscope are shown before and after event selection. For the event selection using the ΔE-E information, each kinematically relevant E-ΔE combination was energy calibrated separately [Ste00], using the deuteron peak and the kinematic relations given in formulae (4.29) and (4.30) for the energy detector and the Bethe-Bloch formula for the ΔE-detector. As can be seen in figure 4.25, the discrimination between deuterons and protons is rather clean. The cut was done with a polynomial which was fitted to a number of selected points. The clean separation between protons and deuterons is confirmed by looking at the time-of-flight spectra, shown in figure 4.26. There, the particle energy is plotted versus the ToF of the particle with respect to an RF signal (TDC signal) for all recorded events (left-hand side) and for events identified as deuterons (right-hand side).

Deuterons belonging to the high-energy solution of equation (4.29) were detected as single events and could be identified by relying on the ΔE-E information, only. The angular range spanned by these deuterons in the centre-of-mass frame of reference is about $30^\circ \lesssim \theta_{\mathrm{cm}} \lesssim 100^\circ$. For the selection of deuterons detected in coincidence with a corresponding proton, more care had to be taken. Especially at scattering angles near $\theta_{\mathrm{lab}} \approx 30^\circ$, the deuteron may belong to either solution of equation 4.29. For a good coincidence event, both outgoing particles have to be co-planar, i.e., the difference between their azimuthal scattering angles should be $\Delta\phi = 180^\circ$. Depending on the laboratory scattering angle of the proton, the low- or high-energy solution of equations (4.29) and (4.30) has to be applied. Especially at laboratory scattering angles of the deuteron $29^\circ \lesssim \theta_{\mathrm{d,lab}} \leq 30^\circ$, where the corresponding centre-of-mass angular region is $105^\circ \lesssim \theta_{\mathrm{cm}} \lesssim 135^\circ$, no clear decision on which solution to choose can be made using the deuteron angle only. Here, the centre-of-mass scattering angle, θ_{cm}, has to be obtained from the proton angle, which is spread over a larger laboratory angular range. Doing this, however, the elastically scattered proton has to be cleanly distinguished from a proton emerging from the deuteron break-up reaction. Because of these complications and considering the time frame defined for this thesis, the decision was made to analyse only the events, in which single deuterons were detected.

In the frame of this feasibility study, only a minor fraction of all acquired data, i.e. $< 10\%$, has been analysed, one of the reasons being that the analysis of all data would have required a thorough and time-intensive energy calibration of the ΔE-E hodoscope for several event files.

4.3.2 Calculation of the Physical Observables

The events collected according to the tracking algorithm described in the last subsection, were binned according to the azimuthal and polar centre-of-mass scattering angles φ and θ_{cm} and corrected for dead-time. The bin-size used was $\Delta\varphi = 3^\circ$ for the azimuthal angle and $\Delta\theta_{\mathrm{cm}} = 4^\circ$ for the centre-of-mass scattering angle. After the event collection, an integration over the

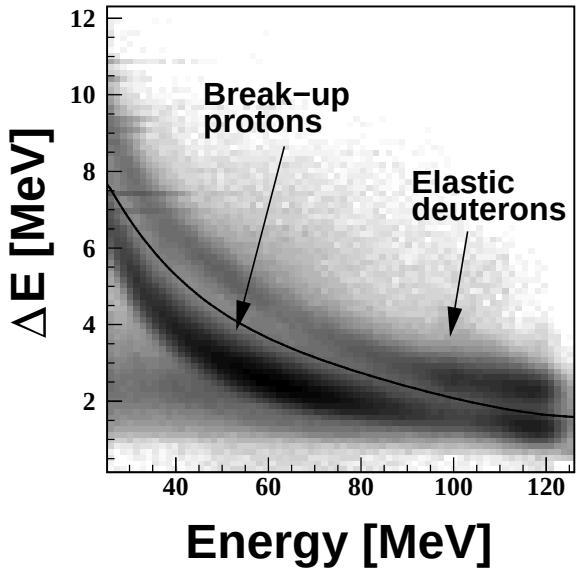

Figure 4.25: Two-dimensional spectrum of the ΔE-E hodoscope of SALAD. The lower band stems from protons, the upper band from deuterons. The black line denotes the cut to select the deuterons.

azimuthal scattering angle φ was performed according to the formulae

$$\begin{aligned} S_L &= \int_{-\frac{\pi}{2}}^{\frac{\pi}{2}} d\varphi I(\theta,\varphi) \\ S_R &= \int_{\frac{\pi}{2}}^{\frac{3}{2}\pi} d\varphi I(\theta,\varphi) \\ S_{LR} &= \int_{-\frac{\pi}{4}}^{\frac{\pi}{4}} d\varphi I(\theta,\varphi) + \int_{\frac{3}{4}\pi}^{\frac{5}{4}\pi} d\varphi I(\theta,\varphi) \\ S_{UD} &= \int_{\frac{\pi}{4}}^{\frac{3}{4}\pi} d\varphi I(\theta,\varphi) + \int_{\frac{5}{4}\pi}^{\frac{7}{4}\pi} d\varphi I(\theta,\varphi) \end{aligned} \tag{4.32}$$

where $I(\theta,\varphi)$ is the number of counts corrected for dead-time in one bin,

$$I(\theta,\varphi) = I_0(\theta)\{1 + k_1\pi p_Z iT_{11}\cos\varphi - k_2 p_{ZZ}T_{22}\cos 2\varphi - k_3 T_{20}p_{ZZ}\}. \tag{4.33}$$

p_Z is the vector and p_{ZZ} the tensor polarisation of the deuteron beam and the constants are

$$k_1 = \frac{\sqrt{3}}{\pi},\ k_2 = \frac{\sqrt{3}}{2},\ k_3 = \frac{1}{\sqrt{8}}. \tag{4.34}$$

The complete evaluation of the integrals in equations (4.32) is given in appendix F. From

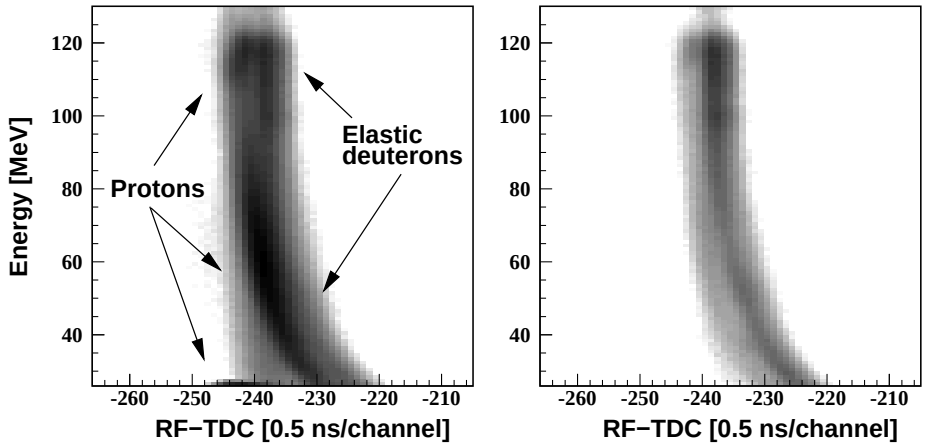

Figure 4.26: Two-dimensional spectra of the particle energy versus its ToF obtained from the signals of the energy detector with respect to the RF (TDC signals). On the left-hand side, the measured energy versus the ToF is shown for all events. On the right-hand side, the same spectrum is shown after the cut on the deuteron band in the ΔE-E spectrum, as shown in figure 4.25, has been made.

these integrals, the vector analysing power iT_{11} can be obtained if $p_{ZZ} = 0$

$$iT_{11} = \frac{1}{2k_1 p_Z} \frac{S_L - S_R}{S_L + S_R} \tag{4.35}$$

and the differential cross section can be obtained from measurements with $p_{ZZ} = 0$,

$$\begin{aligned} I_0(\theta) &= \frac{S_L + S_R}{2\pi} \\ \frac{d\sigma}{d\Omega} &= \frac{I_0(\theta)}{Q\ f(\theta)\ \delta x} \end{aligned} \tag{4.36}$$

where δx is the target thickness and Q the collected charge. The solid angle for a detector covering the full azimuthal angle such as SALAD is given by $\Delta\Omega = 2\pi f(\Delta\theta)$, with $f(\Delta\theta) = \int_{\cos\theta_2}^{\cos\theta_1} d\cos\theta$.

The tensor analysing powers T_{20} and T_{22} can be obtained from measurements done with $p_Z = 0$ and $p_{ZZ} \neq 0$,

$$\begin{aligned} T_{20} &= \frac{1}{k_3 p_{ZZ}} \left\{ 1 - \frac{S_L + S_R}{2\pi I_0(\theta)} \left(\frac{Q}{Q^{p_{ZZ}}} \right) \right\} \\ T_{22} &= -\frac{S_{LR} - S_{UD}}{4\ k_2\ I_0(\theta)\ p_{ZZ}} \left(\frac{Q}{Q^{p_{ZZ}}} \right) \end{aligned} \tag{4.37}$$

where $I_0(\theta)$ is obtained from measurements with $p_{ZZ} = 0$ using equation (4.36) and Q and $Q^{p_{ZZ}}$ are the charges collected during the measurement with $p_{ZZ} = 0$ and $p_{ZZ} \neq 0$, respectively.

Though during the experiment use was made of all possible combinations of the weak and strong fields of POLIS, as given in section 3.1, only a few combinations were eventually used during the analysis. For the calculation of the differential cross section, only events with all fields turned off were used. For the tensor analysing power iT_{11}, only events with pure vector polarisation for which $p_{ZZ} = 0$ were used. To obtain the tensor analysing powers T_{20} and T_{22}, use was made only of events with pure tensor polarisation where $p_Z = 0$.